Dynamic compressive behavior of additively manufactured 17-4 PH stainless steel

by

Siddharth Sriram

A thesis submitted to the Graduate Faculty of
Auburn University
in partial fulfillment of the
requirements for the Degree of
Master of Science

Auburn, Alabama
December 09, 2023

Keywords: Laser Powder Bed Fusion, Fused Filament Fabrication, Split Hopkinson Pressure Bar, Electron Back Scattering Diffraction

Approved by

Dr. Vinamra Agrawal, Chair, Assistant Professor of Aerospace Engineering
Dr. Eldon Triggs, Senior Lecturer of Aerospace Engineering
Dr. Bart Prorok, Professor of Materials Engineering

Abstract

This work focuses on additively manufactured 17-4 PH stainless steel and establishing a correlation between microstructure/printing speed to the dynamic response. Two different methods of additive manufacturing namely Laser Powder Bed Fusion (L-PBF) and Fused Filament Fabrication (FFF) have been employed. The study on L-PBF samples focuses on the role of heat treatment on their dynamic response. Printed samples are subjected to different heat treatment conditions and then to dynamic compression test through the Kolsky compression bar. These samples are examined under electron backscattering diffraction (EBSD) to analyze the texture of specimens before and after impact with and without heat treatment. Additionally, Johnson-Cook (J-C) model is fit to the stress-strain curve to extract their respective plasticity constants. The influence of heat treatment on these material constants during dynamic compression tests is also analyzed. FFF methodology focuses on the influence of printing parameters on the dynamic response. Porosity is an inherent feature during manufacturing. The porosity of the fabricated specimen is examined through X-Ray Computed Tomography (X-Ray CT) and a correlation between porosity and printing speed is established. To observe the effects of printing speed and strain rate on stress-strain response and microstructure, printed specimens are subjected to quasi-static compression and dynamic compression tests through the Kolsky compression bar. The influence of printing parameters, and strain rate on these material constants during dynamic compression test is also analyzed.

Acknowledgments

I would like to extend my deepest gratitude to my advisor, Dr Vinamra Agrawal for their unwavering support, invaluable guidance, and immense patience throughout the course of this thesis. This thesis was only possible because of Dr Agrawal's continuous support during the hardest times in the course of experiments. His constant interaction during every individual meeting and his patient explanation for every question was the key reason for the obtained results. It is incomplete without thanking Dr Eldon Triggs for continuous assistance and support right from the start of the additive manufacturing process. Dr Triggs' simple and practical approach to a problem helped in simplifying most of the issues during manufacturing and helped in saving time. I take immense pleasure in thanking Dr Bart Prorok for being a part of this project and for his constant support in providing facilities, especially EBSD and X-ray CT. Dr Prorok's intense knowledge of materials and mechanics helped a lot in fine-tuning the problem and understanding the problem to a fundamental level.

It's incomplete without thanking my friends from the Department of Materials Engineering. I would like to extend my sincere thanks to Steven, Andrii, Rong, and Tahmina for extending their help with material characterization. I would definitely like to thank Rong and Steven for training me through the process of mounting and polishing and Andrii for sharing his knowledge on the X-ray CT process. I would extend my thanks to Nithin and Julkarnye for extending their help during quasi-static testing. It is incomplete without extending my sincere thanks to the MML family- Alton, Roberto, Vaibhavi, Kaniz, and Amrit for constant inputs during the meeting. I wanted to thank Adithya and Thiraj for constantly backing me up during my low points.

I would extend my wholehearted thanks to my mother for her constant prayers and support throughout this project. Most of all, I would like to thank my wife Swetha for her constant support right from the start of the course. Thank you for standing with me and backing me up throughout this journey.

Table of Contents

List of Figures

List of Tables

Chapter 1

Introduction

Now additively manufactured materials are replacing conventional materials in every field like aerospace, medicine, defense, automotive, and space by their flexibility, cost, quality, and speed and are also advantageous over conventional manufacturing processes in producing extremely complicated shapes [2]. As the usage of AM parts is expeditiously increasing, it is essential to understand the mechanics of such materials under static and dynamic conditions. There are various AM techniques explored by the research community to date for the fabrication of metal parts. Among these techniques, laser powder bed fusion (L-PBF) which is also referred to as Selective Laser Melting (SLM) [37] is one of the directional solidification techniques that is proven to provide higher structural strength and density over complex shapes produced with accuracy [14, 22]. Laser powder bed fusion(L-PBF) was developed in the year 1992 by DTM Corporation, USA [19]. This process is also termed as Selective Laser Sintering(SLS). In SLS, parts are created by partially melting powder and then sintering them in a furnace at a high temperature. Porous structures and ceramics are the ideal candidates for this procedure. For pieces made of thick metal, total melting is favored over the powder sintering process, and technologies entailing the powder's whole melting were created late in the year 2000. Selective laser melting is the process's name (SLM). The SLM procedure happens in a closed inert gas-filled chamber. Pre-alloyed powders are used as feedstocks which range in the particle size of 20μm to 40 μm. Now additively manufactured materials are replacing conventional materials in every field like aerospace, medicine, defense, automotive, and space by their flexibility, cost, quality, and speed and are also advantageous over conventional manufacturing processes in producing extremely complicated shapes [2]. As the usage of AM parts is expeditiously increasing, it is essential to understand the mechanics of such materials under static and dynamic conditions. There are various AM techniques explored by the research community to date for the fabrication of metal parts. Among these techniques, laser powder bed fusion (L-PBF) which is also referred to as Selective Laser Melting (SLM) [37] is one of the directional solidification techniques that is proven to provide higher structural strength and density over complex shapes produced with accuracy [14, 22]. In the L-PBF process, the powders are exposed to a laser source that results in the melting of the metallic powders in a layer-by-layer fashion and gets deposited as a fine layer. L-PBF process provides numerous advantages like shorter lead time, near net shape, higher precision, and accuracy during manufacturing [11]. During AM processes like L-PBF, there arises rapid change in the heating and cooling rate of the sample which has a significant impact on the microstructure of AM samples [38]. Each process parameter has a major contribution towards the microstructure in the AM components. For example, laser density below the optimum level leads to an increase in porosity in the material [7] and increased laser density gives rise to the balling effect [12] which can result in unmelted regions. The power of the laser source and scanning speed are the important parameters that influence the microstructure of the printed AM material. Columnar grains are usually formed along the build direction which leads to anisotropy and degradation of properties [41] and the key objective of researchers is to eliminate columnar grains and replace it with equiaxed grains to enhance mechanical properties [23, 4]. Owing to these heating, cooling, and solidification process, there arises heterogeneity in microstructure in the additive manufacturing process and post-processing of the additively manufactured components are essential to temper these effects [39, 8]. Among the many available post-processing operations like hot isostatic pressing, machining, and surface finishing, heat treatment is widely used to eradicate residual stresses and have control over the microstructure.[46, 44]. However, heat treatment of 17-4 PH steel comes with its challenges. Fe-17Cr-4Ni-4Cu stainless steel which is commonly referred to as 17-4 PH is a precipitation-hardened martensitic stainless steel that offers high corrosion resistance, high toughness, and high strength, enhanced fatigue behavior [3, 31, 9]. Heat treatment of 17-4 PH gives rise to various challenges like heterogeneous grain size distribution coupled with residual stresses during the manufacturing process itself. Many articles have reported results for AM

17-4 PH stainless steel for quasi-static tests considering the effect of process parameters in laser powder bed fusion. Extensive research has been conducted on the fatigue performance of AM 17-4 PH stainless steel [34, 26, 36, 30].

Fused Filament Fabrication(FFF) is a method of the additive manufacturing process that is preliminary derived from the extrusion process [27]. Processes like laser powder bed fusion, and direct energy deposition have very high initial investment costs[42, 29, 1]. Machines used in processes like laser-powder bed fusion, and direct energy deposition process are massive in size and consume enormous amounts of space. These processes owing to thermal history leave residual stresses that alter the microstructure of the material [40]. Whereas, a fused filament fabrication process is simple and easy to operate and the machine is so handy that it can be used as a tabletop printer. The fused Filament Fabrication process was predominantly used for printing plastic parts and extensive research has been conducted on the printing of polymers. Variations of process parameters and their impact on mechanical properties have been explored to a wide range for a variety of polymers like nylon, PLA, PETG, and so on. The FFF process for metals is a modification of two different processes combined in a single process. This process is a combination of the extrusion process and powder metallurgy process. Stage 1 is extrusion and printing of the filament material and stage 2 is where fundamentals of powder metallurgy come into action. The printed part is sintered to remove the polymer binders. The base filament is fabricated from blending of metal feedstock and polymer binder and extruded into a polymer/metal hybrid filament using filament extrusion process[35]. The extruded filament is utilized as an input for the FFF printer for printing the necessary parts. Once the print is done, the component is exposed to a debonding and sintering process to remove the polymer which is blended with the metal feedstock, thus evaporating the polymer and leaving behind the metal. Researchers have extensively explored fused filament of stainless steel, especially 316L steel which has been rigorously researched due to ease of its availability as a commercially available material and its ease of fabrication. [40] have studied the process of fused filament fabrication right from the fabrication of filament to the sintering of the fabricated green part. More emphasis was given to the optimization of the process parameters to obtain the part with the best quality. To be more precise in improving the quality of the printed product, debinding and sintering time was focused more on obtaining parts with the lowest residual stress. It was inferred that by optimizing the debinding and sintering time, the density of the printed part was about 95%. [42] focused more on optimizing the process parameters with commercially available 316L filaments rather than on extruding the base filament from scratch. Response Surface Method(RSM) was chosen for the Design of Experiments(DoE) with parameters like nozzle temperature, layer thickness and flow rate as variables with 8 different print configurations. It was observed that at print configuration 2, the mechanical responses like elastic modulus, and yield strength were higher. [32] have once again focused on 316L stainless steel right from the development of the base filament from scratch to testing their mechanical response. Feedstock is prepared with 316L powders which were 65% by volume and 35% low-density polyethylene (LDPE) was used as a binder. Rheological characterization of the base filament was conducted to understand the flow characteristics of the base material so the input temperature parameters can be fixed to obtain better output in terms of the quality of printed parts. Post-sintering, the densification of 93% was achieved by having the optimum debinding and sintering phase. Mechanical characterization like hardness test, and tensile test from which its yield strength and ultimate tensile strength are obtained and are in comparison with other metal additive manufacturing processes. It was also stated that the difference in the properties was due to the porosity which was inherent during the printing of the sample. [6] have emphasized on variation of nozzle diameter, line width, layer thickness, and feed rate as process variables maintaining the pattern and density of infill as a constant. Tensile tests were conducted on specimens with variations in the orientation of the samples. Another well-explored grade of steel is 17-4 PH stainless steel for ease of filament fabrication and commercial availability. [20] have compared two different commercially available 17-4 PH base filaments from markforged manufactured by atomic diffusion additive manufacturing(ADAM) and BASF ultrafuse which was fused filament fabrication (FFF). Tensile samples were printed with two different 17-4 PH filaments with different build orientations and subjected to tensile testing. Hardness and porosity were also measured and it was inferred that markforged samples produced better densification up to 98% which was higher than that of ultrafuse samples that were about 89%-95%. This observation proves FFF process has porosity which is inherent in the manufacturing process. [25]

have tried to understand the post-processing routes to improve the print quality and analyze the tribological behavior of 17-4 PH stainless steel fabricated via the fused filament fabrication process. The fabricated specimens were exposed to surface mechanical attrition treatment (SMAT) and magnetron sputtered gum metal (GM) coating with a combined combination of 4. Dry slide wear and corrosion experiments were conducted on the samples. Porosity was a key element influencing wear behavior. These porosities acted as locations for stress concentration and both abrasion and adhesion wear phenomena were observed. On the other hand, SMAT and GM coating improved the corrosion resistance of the material. [28] emphasized the bio-fouling behavior of additively manufactured copper through fused filament fabrication methodology. [43] concentrated on the printing of copper/PLA filaments through the fused filament fabrication process and the printed material's electrical conductivity was ascertained. Several parameter sets were assessed using an experiment design that varied the extruder temperature and printing speed. After that, cuboids were created using the chosen parameter set to ascertain the electrical conductivity and an ideal coil design. One of the investigated filaments allowed for the printing of the coil in two sizes—the original and a factor of two—but the other filament did not allow for this since the printed material was not dimensionally stable with the chosen process parameter set. [15] focused on the quasi-static and dynamic behavior of PLA and copper-filled PLA. Stress-strain curves were obtained for varying strain rates. The micro-morphology of the dynamic impact section and the quasi-static compression fracture were examined using scanning electron microscopy (SEM). The two materials' yield stress and elastic modulus both rose as the strain rate increased, according to the results. When compared to a material subjected to quasi-static loading, the material subjected to dynamic loading had a considerably higher strength. Copper powder was uniformly distributed throughout the 3D-printed sample, according to the PLA-Cu material's SEM image. Stress first concentrated at the defect site, which corresponded to the interface between the copper powder and PLA matrix, leading to comparatively lower toughness. This result was in line with the high-speed photography photos, which verified that the specimen was destroyed along with an explosive crushing procedure. In addition, a viscoelastic constitutive model of the material was established by fitting the experimental data using a Zhu–Wang–Tang constitutive model. The available literature has mostly focused on understanding the quasi-static behavior of the material fabricated through the fused filament fabrication process. When working on the fused filament fabrication process, porosity becomes an inherent part of the course of manufacturing the material. So the obtained stress-strain curve, Young's modulus, yield strength, and strain hardening behavior depend on the percentage of porosity, position, and size of the porosity.

In this work, we will be focusing on dynamic testing on AM 17-4 PH stainless steel with and without the effect of heat treatment and quasi-static and dynamic compression test for 17-4 PH stainless steel fabricated by fused filament fabrication using a Split Hopkinson pressure bar equipment. We will be obtaining the constants for Johnson-Cook(JC) flow stress models from the dynamic stress-strain curve. Johnson-Cook (JC) elastic-plastic model is one of the most widely used constitutive models in the FE modeling community. [21, 33] have worked on the methods to extract the parameters for the JC model. Fox et al [10] have extracted the constants for the JC model for additively manufactured 17-4 PH stainless steel under dynamic tensile and compressive conditions. As JC is an empirical model, they exactly do not replicate the physics of deformation. The influence of heat treatment on AM 17-4PH steel concerning the dynamic test and its correlation with the flow stress behavior and the constants for the constitutive models are obtained. This work also focuses on the relationship between heat treatment, grain structure, and its impact on stress-strain behavior.

Chapter 2

Manufacturing Methods

2.1 Laser Powder Bed Fusion(LPBF)

Figure **??** gives a detailed schematic of the laser powder bed fusion process. The state-of-the-art additive manufacturing technique known as Laser Powder Bed Fusion (LPBF) works by a well-planned sequence of stages. Initially, a precisely regulated layer of fine metal powder is applied throughout the build platform using a recoating mechanism. The main instrument for selectively melting and fusing the metal powder by the cross-sectional pattern of the desired 3D product is therefore a high-power laser, usually a fiber laser. Based on the digital instructions supplied by computer-aided design (CAD) data, the laser's energy output is precisely controlled, guaranteeing the precise and regulated melting of the prescribed locations. Then the procedure moves onto the layer-building and solidification stage, where the CAD model serves as the only source of guidance for the laser's motions. The material is gradually melted and fused as the laser moves across the powder bed, creating a layer that solidifies. The construction platform is lowered by the amount of the necessary layer thickness to construct the 3D item, and each new layer of powder is evenly distributed over the one that came before it. Each layer progressively bonds to the one below it in an iterative process that continues, producing the entire item from the foundation upwards. Once printing is complete, the item is left to cool inside the powder bed. After the cooling phase, the finished item is carefully removed, removing any leftover, unmelted powder. Post-processing procedures including heat treatment, support structure removal, and surface finishing may be required to maximize the part's mechanical qualities and appearance, depending on the application and particular requirements.

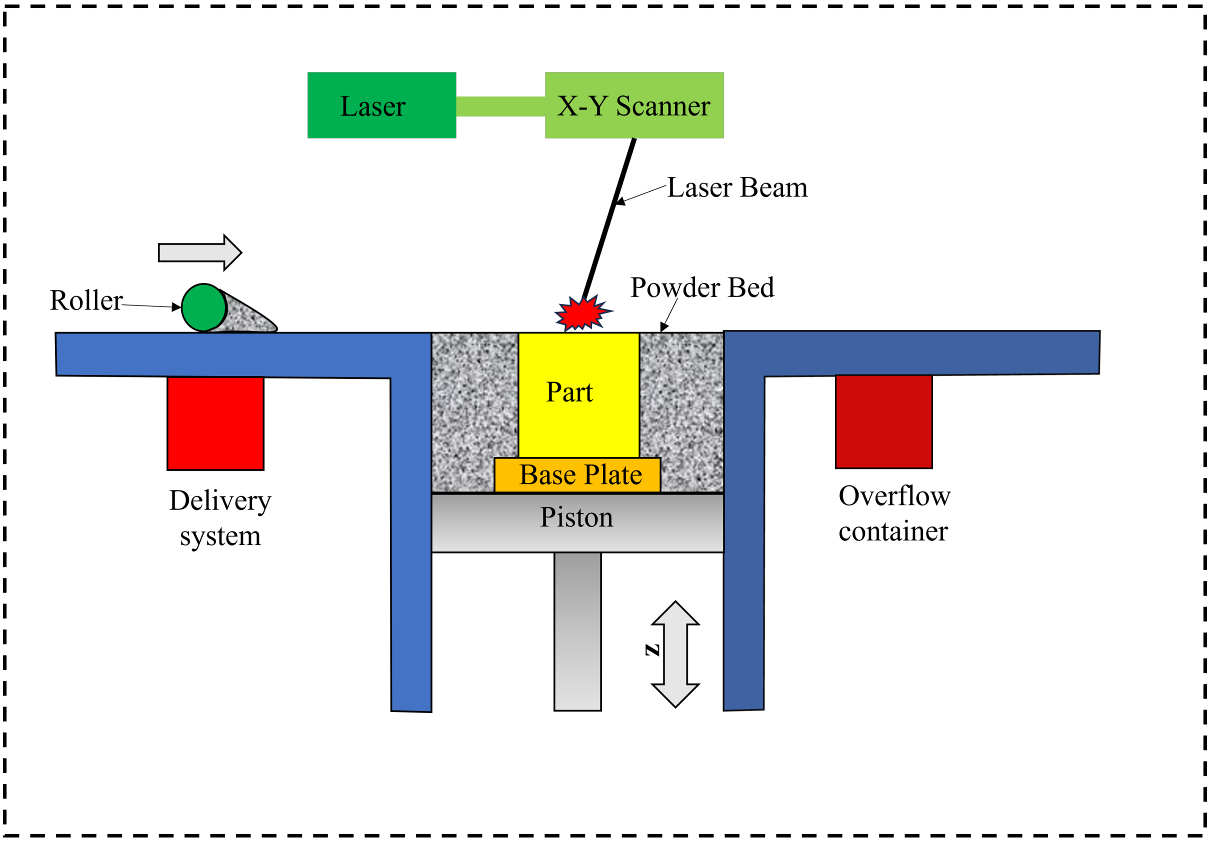

Figure 2.1: Schematic of Fused Filament Fabrication process

The chemical composition of 17-4 PH stainless steel utilized in this experiment is given in Table 2.1 below [36]. Laser Powder Bed Fusion(L-PBF) methodology was utilized for the fabrication of 17-4 PH stainless steel using the EOS M290 machine. The parameters used for the fabrication of 17-4 PH stainless steel is listed in table 2.1 [36]. Argon was the shielding gas used during the manufacturing of 17-4 PH stainless steel where the printing direction was vertical.

Table 2.1: Material constituents

Constituents	C	Cr	Ni	Cu	Mn	Si	Nb
Wt %	0.01	15.6	4.033	3.89	0.24	0.29	0.33
Constituents	Mo	N	O	P	S	Fe	
Wt %	$<$ 0.01	0.01	0.05	0.004	0.003	Bal.	

The specimen of dimension 4.97mm x 30.31mm x 24.94mm was the outcome of printing from the L-PBF process. For the dynamic compression test, specimens were cut using the wire

Table 2.2: Laser Powder Bed Fusion Parameters

Laser Power (W)	Scanning speed (mm/s)	Hatching space (μm)	Layer Thickness (μm)
220	755.5	100	40

EDM process for a dimension of 5mm x 5 mm x 5 mm. Therefore these cubical specimens were utilized for the dynamic compression test. Before the dynamic compression test, the printed 17-4 PH stainless steel samples were heat treated to observe the effect of heat treatment on the microstructure. Four different cases were considered for heat treatment which resulted in each heat treatment resulting in different dynamic stress-strain responses. To understand the role of heat treatment in the microstructure and dynamic stress-strain response, the printed samples were subjected to different heat treatment conditions. As per ASTM standards, there are different heat treatment procedures recommended for 17-4 PH stainless steel. Owing to the unique characteristic of precipitation hardening, each case of heat treatment results in different mechanical properties upon observation. To examine the effect of heat treatment on dynamic stress-stress behavior of 17-4 PH stainless steel, heat treatment at different conditions is carried out which are listed in table 2.1 below.

Table 2.3: Heat treatment parameters

S.No	Temperature °C	Duration (Hours)	Quenching Environment
1	482	1	Air cooled
2	552	4	Air cooled
3	1050	0.5	Air cooled
-	482	1	Air cooled
4	1050	0.5	Air cooled
-	552	1	Air cooled

2.2 Fused Filament Fabrication(FFF)

The general schematic of the fused filament fabrication process is described in Figure 1. It consists of a spool containing the polymer/metal hybrid filament. The filament is fed to the nozzle through a roller which sends the material to the nozzle which has a heating element embedded into it. When the material inside the nozzle starts to heat up, the solid hybrid filament starts plasticizing due to the temperature effect, ready to flow. The flow rate of the material can be varied according to the requirement. The nozzle element is capable of moving in positive and negative x and y directions. The material which flows out of the nozzle starts getting deposited on the print bed which also has a heating element. The material starts getting printed according to the geometry given as an input to the system. The plasticized hybrid filament gets deposited layer-by-layer until the desired geometry is achieved. The print bed is capable of moving in the positive and negative z direction. The parameters which are responsible for the printing of material are, % infill of metal, print speed, nozzle temperature, print-bed temperature, and flow rate. Once the material is printed, the green part is placed in a chamber for debinding the solvent, and the next stage is the sintering process. Here in the sintering process, the material is placed inside a furnace where the polymer in the green part evaporates shrinking the metal left behind.

The material used for the fused filament fabrication process was commercially produced and was acquired from BASF. The BASF filaments are fabricated using a filament extrusion process where the binder material is a patented material by BASF and the particles are 17-4 PH stainless steel. Fused Filament Fabrication(FFF) methodology was utilized for the fabrication of 17-4 PH stainless steel. The polymer/metal hybrid filament which is commercially acquired from BASF technologies is fed as an input into the nozzle which has an inbuilt heating unit. The heating unit plasticizes the hybrid polymer/metal filament allowing it to flow during the printing process.

Table 2.4: Printing parameters

S.No	Parameter	Unit	Value
1	Printing speed	mm/min	40
2	Print Bed Temperature	°C	70
3	Nozzle Temperature	°C	250
4	Infill percentage	-	100

The printing parameters were chosen purely by varying the combination of print speed, print bed temperature, and nozzle temperature. The experiments were conducted in Ultimaker S5 printer. The print speed of the machine was restricted between 15-50 mm/min. Beyond the print speed ended up with clogging of the print head so print speed was chosen as 40 mm/min respectively. Increasing the print bed temperature beyond 80 °C created debonding between the print bed and the surface of the specimen which failed the specimen. So the print

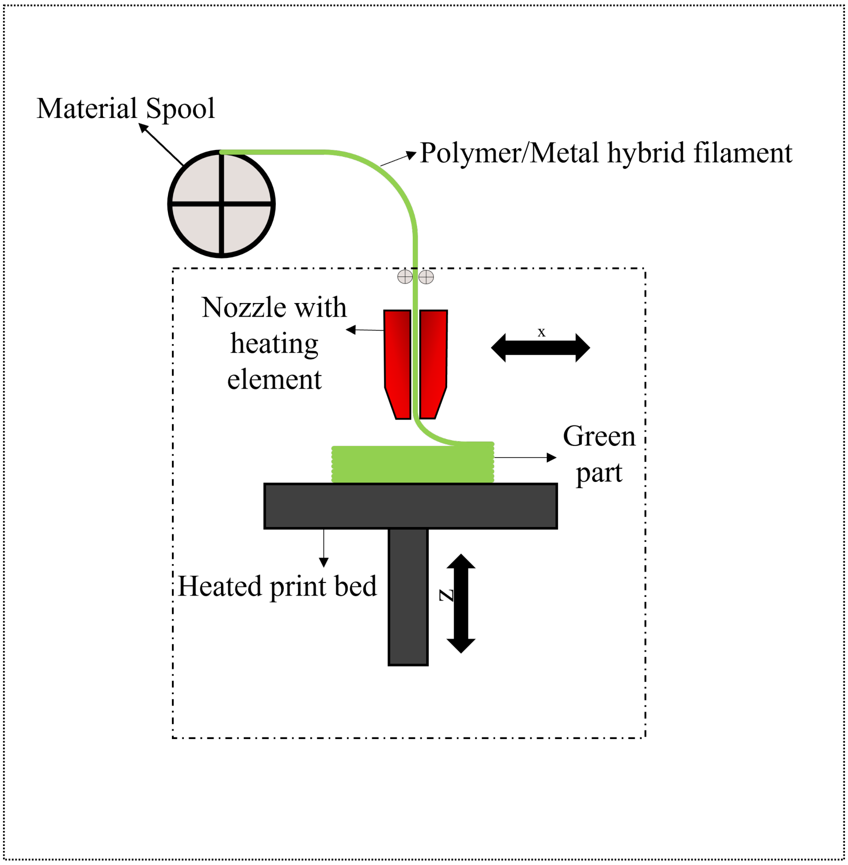

Figure 2.2: Schematic of Fused Filament Fabrication process

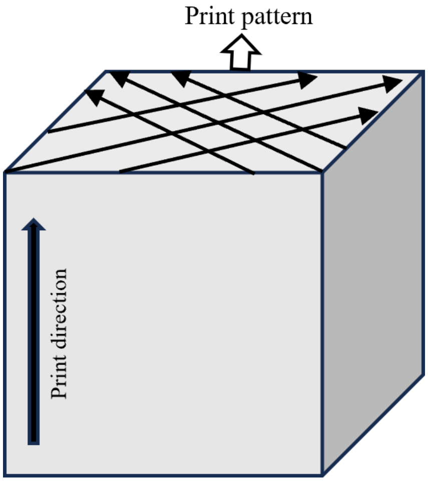

Figure 2.3: Schematic of Fused Filament Fabrication process

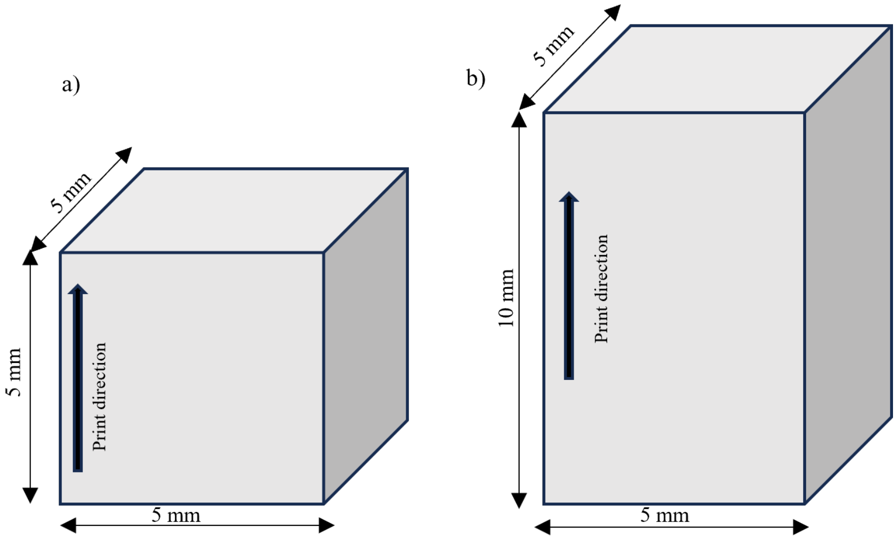

Figure 2.4: Schematic of Fused Filament Fabrication process

bed temperature was restricted to a single value of 70 °C. Nozzle temperature has a greater influence of the flow of material. Increasing the nozzle temperature above 250 °C increases the fluidity of the material breaking the polymer bonds before sintering. Below 250 °C, it makes it hard for the flow of the polymer/metal hybrid filament as it hasn't reached the adequate temperature. So nozzle temperature was fixed at 250 °C. Infill % was maintained at 100% to get the material with the least porosity.

For the printing process line pattern has been adopted as a printing strategy for all the samples. The printed part with the polymer/metal hybrid system before sintering is called the green part. The dimensions of the green part for the dynamic compression test are about

2in x 2in x 2in as shown in figure 2.3. The specimens are intentionally printed oversize as they undergo a reduction in dimension during the sintering process for both quasi-static and dynamic compression test samples so later they can be machined out. After printing, the specimens are sent for sintering where the specimen is placed in a furnace during the sintering process the polymer evaporates due to the temperature in the furnace compacting the metal particles inside the polymer and obtaining the final part. Figure 2.4 describes the samples for quasi-static and dynamic compression test For dynamic compression, test specimens were cut using wire EDM process for a dimension of 5mm x 5 mm x 5 mm. and 5mm x 5 mm x 10 mm for varying the strain rates. Therefore these cubical specimens were utilized for the dynamic compression test and the cylindrical specimens were used for the quasi-static compression test.

Chapter 3

Mechanical Testing

3.1 Quasi-static compression

A quasi-static compression test is to understand the compressive behavior of any material under quasi-static loading. Here the strain rates are usually very low at the rate of $10^{-3}s^{-1}$ to $1s^{-1}$ varying on material to material. Figure 3.1 describes the experimental set-up of the quasi-static compression experiment.

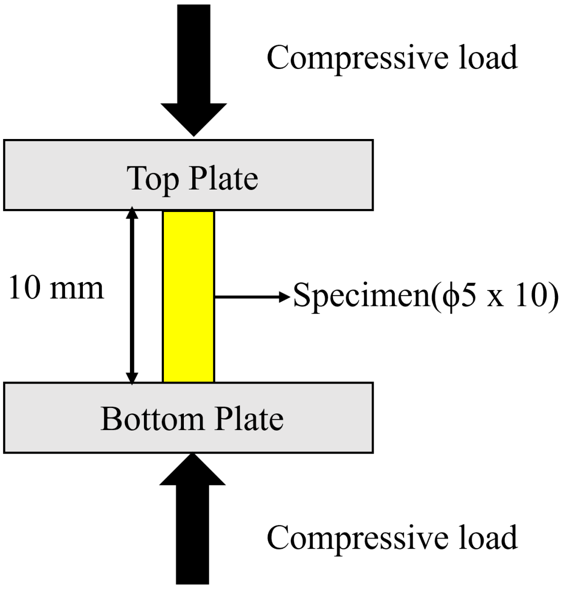

Figure 3.1: Schematic of Quasi-static compression experiment

The experiments are conducted on an INSTRON machine with a load cell capacity of 100 kN. The specimen initially were chosen according to ASTM E9 standards with a diameter of 30 mm and a length of 25 mm making the L/D ratio of 2. However owing to the limitation of loadcell, there was not much deformation observed on the specimen. Then the specimen with an L/D ratio of 2 was chosen according to the ASTM E9 standard which had a diameter of 13 mm and length of 25 mm. Again it sustained very little deformation which showed very little deformation and the same was reflected in the force-displacement curve obtained during the experiment. To visualize the deformation in the specimen, the specimen was scaled down with the same L/D ratio of 2 with a diameter of 5 mm and length of 10 mm. The sample of diameter 5 mm and length 10 mm were prepared and cut from the block printed at the speed of 40 mm/min using a fused filament fabrication process. The samples were cut for the required dimension using electric discharge machining from the bulk sintered sample printed at 40 mm/min [13] The uniaxial compression test was carried out using servo controlled universal testing machine at a strain rate of $1s^{-1}$. Our interest lies in seeing the effect of strain rate when transitioning from quasi-static to dynamic compression test and observing the effect of strain rate in the grain orientation which is observed under electron backscattering diffraction. The compressive mechanical properties are investigated based on the average of five samples.

3.2 Dynamic Compression test-Kolsky bar

Dynamic compression test is usually performed using a Kolsky Bar which is also called a split hopkinson pressure bar(SHPB) is a tool for characterizing the mechanical response of a material under higher strain rate in the order of $10^2s^{-1} - 10^4s^{-1}$. The approach of testing the dynamic response of a material placed between two elastic rods was first experimented with by Kolsky in 1949 [18]. His approach was instead of directly impacting the specimen, the specimen placed between two elastic rods is hit with an explosive impact on one bar called as incident bar and the other bar called as transmission bar. This design creates and propagates a compressive stress wave when the incident bar is loaded by an external impact, such as a hammer strike. Bar material is moved in the direction of the specimen as it passes by. At the point where the wave meets the interface between the the specimen and the incident bar, some of the wave is reflected back into the incident bar around the impact point, with the remaining data traveling through the exemplar through the transmission bar. Different strain rates can be obtained by adjusting the specimen size and impact velocity. Additional examination of the waves captured during the impact event yields details about the loading circumstances and deformation stages within the specimen. This system, which Kolsky first presented in 1949, has been referred to as the Kolsky bar or, as he later clarified, a split-Hopkinson pressure bar (SHPB).

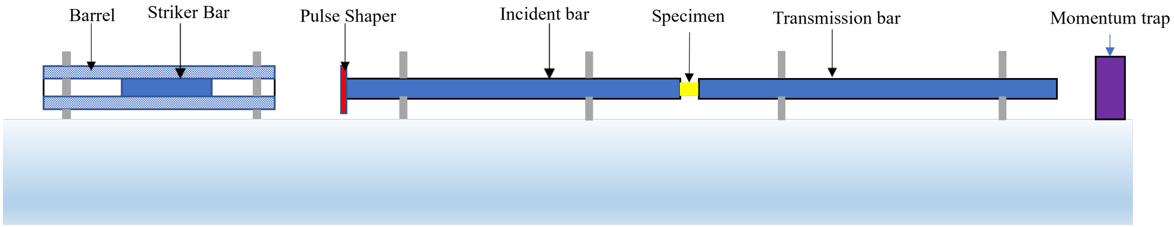

Figure 3.2: Schematic of Split Hopkinson Pressure Bar(SHPB) setup

Figure 3.2 describes the construction of a Kolsky compression bar setup. The setup consists of a loading component, a bar component, data acquisition system. The case we are considering is the dynamic loading scenario. The striker bar is loaded inside the barrel with venting holes drilled to ensure impact at a constant speed. The barrel is connected to a gas tank which is coupled to an air compressor. The other two bar elements are the incident and transmission bar. The incident, transmission, and striker bars are usually made out of the same material from the same batch of samples. It is intended that the bar material be linearly elastic with a high yield strength since surface strains are used to measure the stress waves inside the bars. The bars must be physically straight and able to move freely on their supports with the least amount of friction to guarantee one-dimensional wave propagation in the bars. The loading axis of the bar system is the common straight axis along which the entire system must be perfectly aligned. To prevent overlapping between the incident and reflected pulses, the incident bar needs to be at least twice as long as the striker. The incidence and transmission bars are positioned between the specimen. To quantify bar strains in Kolsky-bar investigations, strain gauges have become the industry standard. Normally, a bar diameter is crossed by two strain gauges that are symmetrically connected to the bar surface. A Wheatstone bridge conditions the signals obtained from the strain gauges. The voltage output from the Wheatstone bridge is typically on the order of millivolts in a typical Kolsky-bar experiment, with a small amplitude.

When the striker bar is fired, the striker bar impacts the incident bar and generates elastic stress waves that propagate through the incident bar. The incident waves when coming in contact with the material sample, a part of the waves get transmitted through the sample to reach the transmission bar, and the rest gets reflected. Strain gauges are placed on the incident and the transmission bar that measures the strain that helps us to calculate the nominal value of strain, stress, and strain rates with the following equation. [5]:

$$\sigma(t) = \frac{A_B}{A_s} E_B \epsilon_T \tag{3.1}$$

$$\epsilon(t) = (-2\frac{C_B}{L_s}) \int_0^t \epsilon_R \, dx \tag{3.2}$$

$$\epsilon'(t) = (-2\frac{C_B}{L_s}) \epsilon_R \tag{3.3}$$

Here A_B and A_s are a corresponding cross-sectional area of bars and specimens respectively. E_B is the elastic modulus , C_B is velocity of the wave. L_s is the sample's initial length and t is its corresponding time. Also, ϵ_R and ϵ_T are reflected and transmitted waves that are recorded through the strain gauges which are mounted on the incident and the transmission bars. True stress, strain, and strain rate are calculated using the following equation

$$\sigma = \sigma(t)(1 - \epsilon(t)) \tag{3.4}$$

$$\epsilon = -ln(1 - \epsilon(t)) \tag{3.5}$$

$$\epsilon' = \frac{\epsilon'(t)}{(1 - \epsilon(t))} \tag{3.6}$$

In our case with laser powder bed fusion samples, our interest is to understand the effect of heat treatment on the dynamic compressive behavior of additively manufactured 17-4 PH stainless steel at a constant strain rate. The dynamic compression test of L-PBF 17-4 PH stainless steel specimens was investigated using a Split Hopkinson Pressure Bar (SHPB) setup for both heat-treated and non-heat-treated 17-4 PH specimens. Square shape samples of dimensions 5 mm x 5 mm x 5 mm are used for the dynamic compression experiment. For every experiment, the loading happens parallel to the printing direction. The experiments were conducted at room temperature and five experiments were conducted to ensure repeatability. For the case of the fused filament fabrication process, our interest lies in the effect of strain rate. Strain rate variation is achieved during the experiment by varying the length of the specimen. Two different specimens were cut out from the block printed at 40 mm/min. Specimen of dimensions 5 mm x 5 mm x 5 mm and 5 mm x 5 mm x 10 mm are chosen for conducting dynamic compression experiments with varying strain rate The setup consists of three main components. Striker bar, Incident bar, and Transmission bar which are made up of C350 maraging steel. The barrel is connected to a gas tank which is in turn coupled with an air compressor where the gas tank can store compressed air. A momentum trap is installed at the end of the transmission bar to stop the transmission bar from moving out of the experimental range. A copper shim of 0.5 mm thickness is used as a pulse shaper to smoothen the output from the strain gauges. The dimension of the whole setup is described in table 3.2 below

Table 3.1: Components and materials

S.No	Component	Material	Dimension in mm (with alternative units)
1	Striker bar	C350 Maraging steel	457.2 (18 inches)
2	Incident bar	C350 Maraging steel	1828.8(6 feet)
3	Transmission bar	C350 Maraging steel	1828.8(6 feet)
4	Pulse shaper	Copper(LPBF), Brass(FFF)	0.5

Chapter 4

Johnson-Cook Model

The Johnson-Cook relation is an empirical model derived based on observation of the experimental flow stress curves over a wide range of strain rate and temperature and it lacks any physical basis[16, 45]. Equation 1 describes the flow-stress behavior of the Johnson-Cook model considers strain hardening, strain rate hardening, and temperature softening as independent terms and it does not consider the coupled effect of strain, strain rate, and temperature[45]

$$\sigma = [A + B(\epsilon_P)^n](1 + Cln(\epsilon'^*))[1 - (T')^m] \tag{4.1}$$

where

$$\epsilon'^* = \frac{\epsilon'}{\epsilon'_{ref}} \tag{4.2}$$

$$T' = 1 - \frac{T - T_{ref}}{T_m - T_{ref}} \tag{4.3}$$

Though it is not a physics-based model it is still widely utilized because of the availability of constants for various materials and it also has a simple mathematical form that is easier to implement in FE codes. In the Johnson-Cook model, A represents the yield stress, B and n represent strain hardening, C captures the strain rate sensitivity, and m is the thermal softening exponent. ϵ_p corresponds to plastic strain, $epsilon'$ and ϵ'_{ref} are respectively the actual strain rate and the user-provided reference strain rate. T, T_{ref}, and T_m are respectively the workpiece temperature, reference temperature, and workpiece melting temperature. The JC model parameters are mostly calibrated by utilizing the constitutive data generated using the split Hopkinson pressure bar tests (SHPB) which is capable of testing the material strength at high rates of loading. Johnson-Cook model is purely an empirical model and its application is widespread from metal forming simulations to impact analysis [13]. The advantage of a Johnson-Cook model is the number of constants required to fit a model. JC model requires only 5 material constants to fit the stress-strain curve to the equation.

Chapter 5

Results and Discussion:

5.1 Dynamic Compressive Behaviour for Laser Powder Bed Fusion samples:

The additively manufactured 17-4 PH stainless steel is subjected to dynamic compression using Split Hopkinson Pressure Bar (SHPB) setup for as printed and heat treated 17-4 PH stainless steel.[3] The experiments were conducted at a constant strain rate of 1500 s^{-1} at room temperature and every experiment was repeated five times to ensure repeatability. Figure 2 describes the dynamic stress-strain behavior of additively manufactured 17-4 PH stainless steel. The data acquired from the oscilloscope was converted into engineering stress-strain data. But we do need to focus on the true stress-true strain data which requires conversion of engineering stress-engineering strain data to true stress-true strain data. The engineering stress-engineering strain data is converted using the equations 7 and 8.

$$\epsilon_{True} = ln(1 + \epsilon_{engg}) \tag{5.1}$$

$$\sigma_{True} = \sigma_{engg}(1 + \epsilon_{engg}) \tag{5.2}$$

For no heat-treated case, during the dynamic compression test, there was a reduction in the elastic modulus. This phenomenon was portrayed by [10] where both quasi-static and dynamic scenario was tested. It was stated that there was a reduction in elastic modulus during the dynamic compression test compared to the test conducted from the quasi-static test. So this proves the fact that elastic modulus is strain rate dependent.

Figure 5.1 gives a detailed description of the stress-strain response of additively manufactured

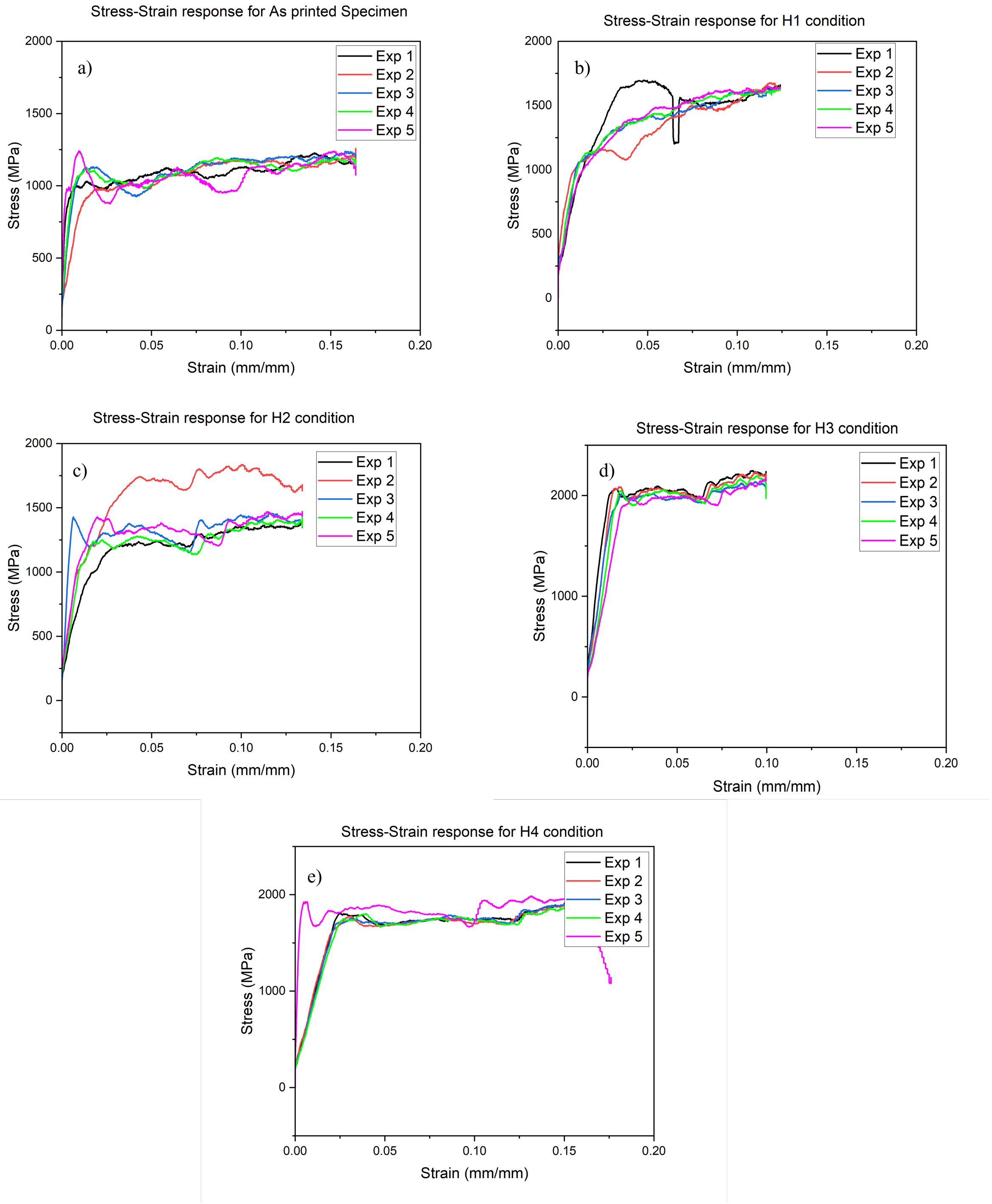

Figure 5.1: Stress-Strain response for a)As printed condition b) H1 Heat treatment c)H2 Heat treatment d)H3 Heat treatment e)H4 Heat treatment

17-4 PH stainless steel with and without heat treatment. A total of 5 experiments were conducted in each case to ensure repeatability. All specimens were cut out from a single block and then were heat treated according to their conditions. So the variation in the stress-strain curve within the conditions may be because of samples cut from different positions. Figure 5.1a portrays the as printed no heat treated condition. As explained most of the experiments had a similar slope region. The variation was observed widely within the conditions in the plastic region. The linear region was isolated for all experiments to estimate the elastic modulus. And yield strength is calculated using 0.2% offset method.

Table 5.1: Variation in yield strength with change in heat treated condition

S.No	Heat treated condition	Yield strength	% Increase/Decrease
1	NH	951.75 ± 39.92	-
2	H1	1190.4 ± 304.68	25.07
3	H2	1263.6 ± 116.16	32.76
4	H3	2012.1 ± 37.68	111.4
5	H4	1747.8 ± 49.9	83.64

Table 5.1 describes the variation in yield strength across the heat-treated conditions. In heat treatment H3 and H4 while observed under an optical microscope to determine the build direction, at that condition the material was completely recrystallized. So determining the build direction was not possible and the impact was not ensured to be performed along the build direction. For the as-printed, H1, and H2 conditions the melt pools were visible under an optical microscope so the impact was done along the print direction. From the true stress-true strain curve, it is seen that the yield strength of the material to the heat treatment done on the printed sample. However, with printed samples, the inherent manufacturing defects like porosity, and voids are not eliminated. So during the dynamic compression test, the degradation in the yield strength is reflected as the region of voids serves as the initiation region for failure to occur. However, as we do post-processing techniques like heat treatment with variations in temperature and time, the yield strength increases. Heat treatment cycles are described in Table 3. For heat treatment condition H1, there is an increase of 25% in the yield strength compared to the non-heat treated as printed counterpart. similarly, there is a significant rise in the yield strength when heat treated at conditions H2, H3, and H4 respectively. There was a 32% increase in yield strength for the H2 heat treatment condition compared to the as-printed case. But when heat treated at H3 and H4 conditions, the yield strength almost doubled. This phenomenal increase was especially because of recrystallization. The mechanism of heat treatment and recrystallization is explained by Karthik et al [17]. During laser powder bed fusion, the manufacturing

happens in deposition in a layer-by-layer fashion. The additively manufactured samples have cellular dislocation structures which enhances the yield strength of additively manufactured samples. During heat treatment, precipitates are formed which enhances the yield strength of the sample.

5.1.1 Extraction of Johnson-Cook constants

Johnson-Cook constants are extracted for heat treating and as printed conditions from the true stress-true strain data from the SHPB test. For the case of laser powder bed fusion, experiments are conducted at constant strain rate and temperature. So Johnson-Cook model can be simplified using the following steps There are a few steps required while evaluating the Johnson-Cook material constants.

- As the experiments were conducted only at room temperature conditions, temperature variation is zero. So the temperature terms can be ignored. Now the equation narrows down to
$$\sigma = [A + B(\epsilon_P)^n](1 + Cln(\epsilon'^*))$$
- Sample size for every experiment was maintained at a constant. So the strain rate sensitivity term also gets reduced. This narrows down the equation to
$$\sigma = [A + B(\epsilon_P)^n]$$
- The above equation is simple to solve as A parameter being the yield strength which can be interpreted from the stress-strain curve
- Plot the true stress-true strain curve after converting them from engineering stress-engineering strain data.
- Determine the yield strength by 0.2% offset method. This gives us the parameter A required for the equation.
- Extract the plastic part of the stress-strain curve.

- Now the equation can be reduced to

$$\sigma - A = B(\epsilon_P)^n$$

$$ln(\sigma - A) = ln(B(\epsilon_P)^n)$$

- Here $ln(\epsilon_p)$ is plotted along x-axis and $ln(\sigma - A)$ along the y-axis. The slope of the curve gives us parameter n and the intercept gives us $\ln B$. By taking the exponential of the term, B can be extracted.

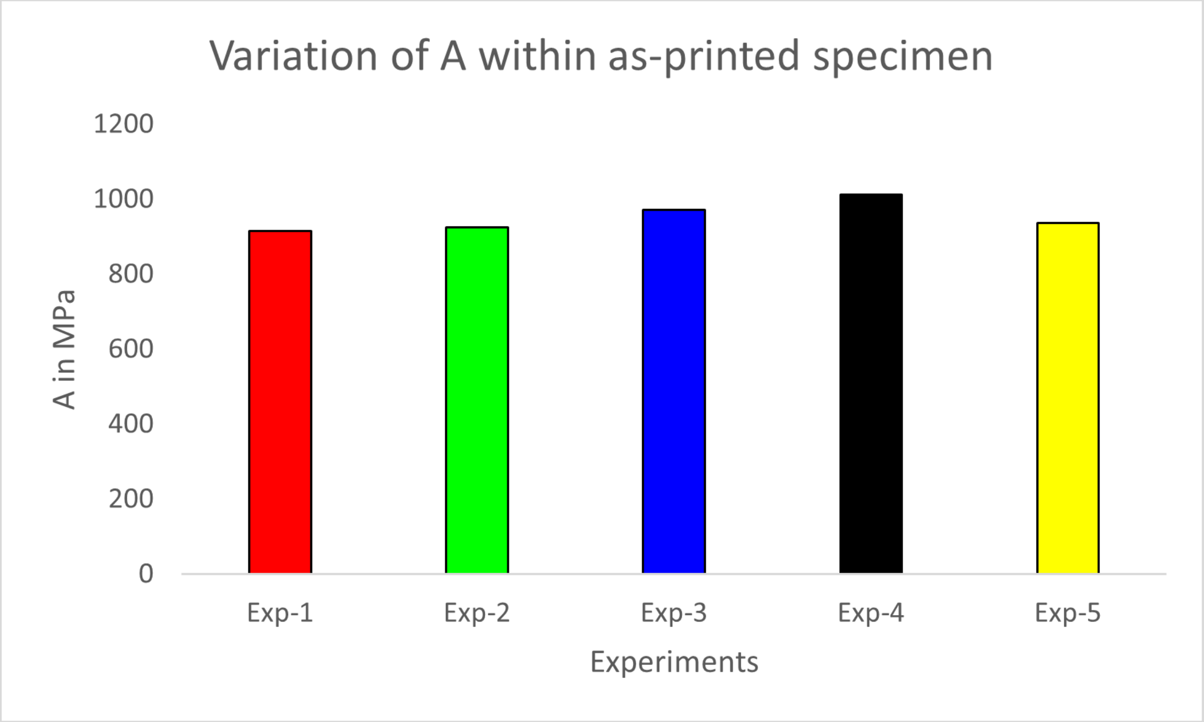

Figure 5.2: Variation of Yield strength for As-printed condition

Figure 5.2-Figure 5.6 describes the variation of yield strength with a change in heat treatment. Figure 5.2 depicts the variation of yield strength within the five experiments conducted on as-printed samples. As our intentions are focused on finding the constants from the flow stress curve, yield strength for every respective experiment is calculated from the true stress-true strain curve using the 0.2% offset method. For as-printed samples, the variation within the experiments was not high. Repeatability was assured for as-printed samples. Exposing the specimen, to heat treatment, there occurs improvement of mechanical properties which are

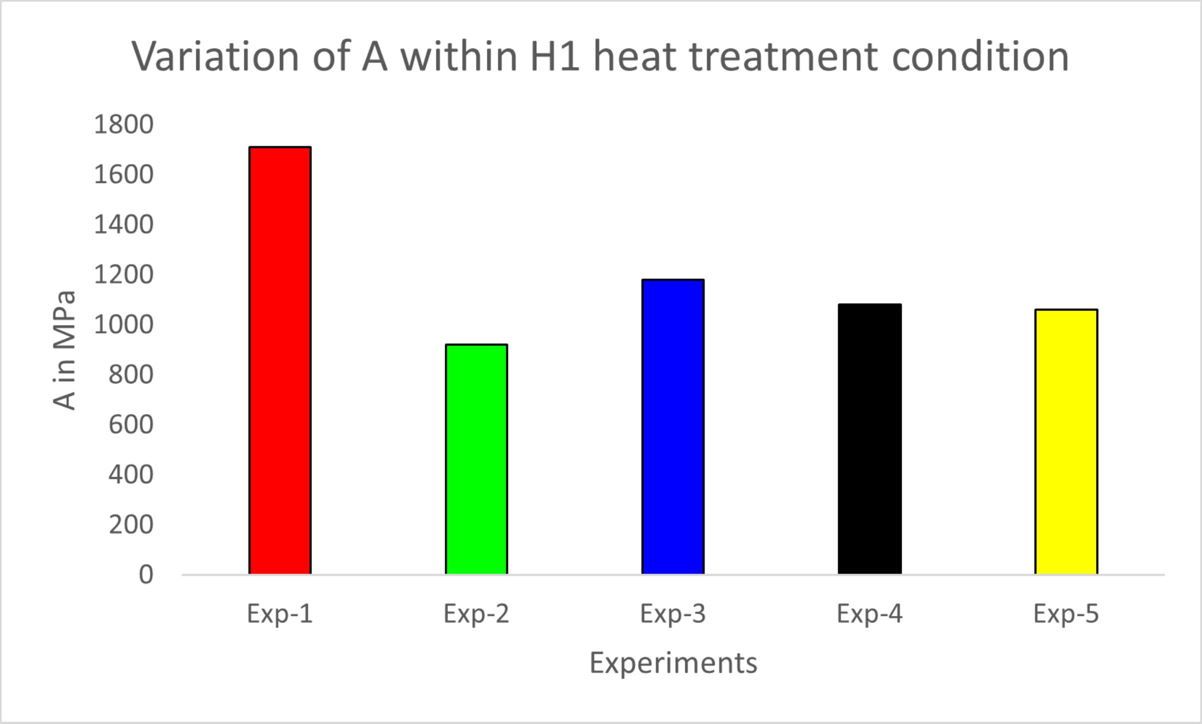

Figure 5.3: Variation of Yield strength for H1 heat treatment condition

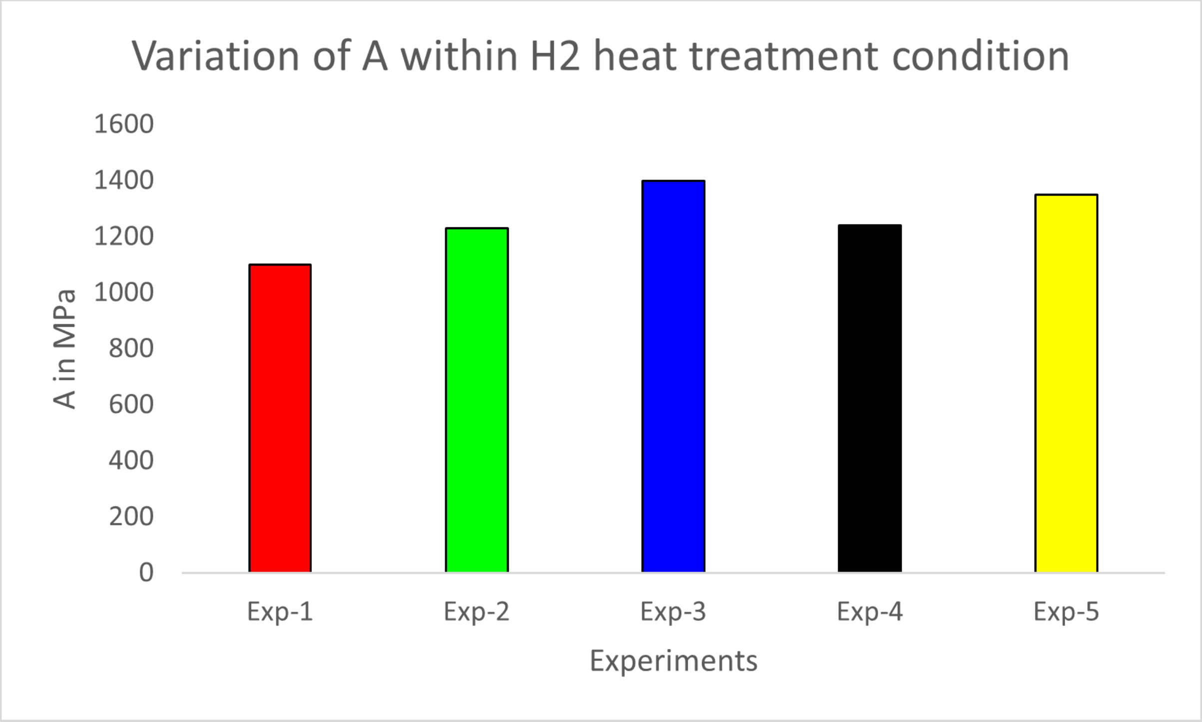

Figure 5.4: Variation of Yield strength for H2 heat treatment condition

observed in the dynamic compression test. As 17-4 PH stainless steel is precipitation-hardened steel, the occurrence of precipitates in the grain boundaries starts to develop with changing

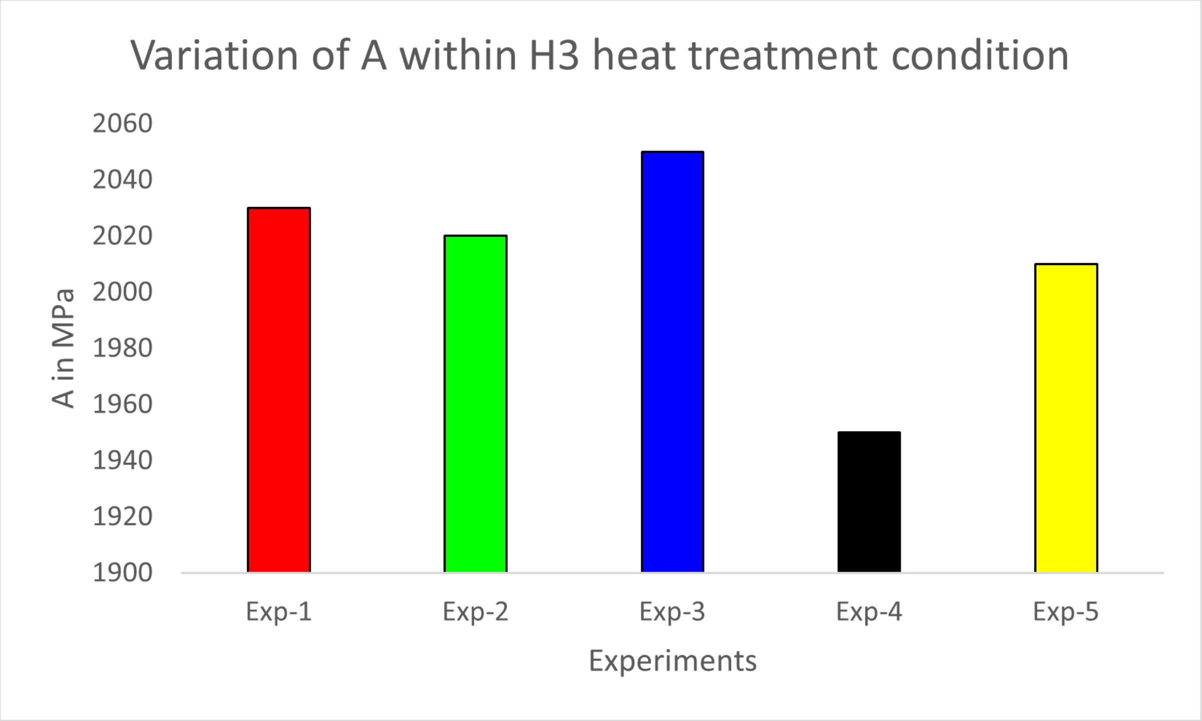

Figure 5.5: Variation of Yield strength for H3 heat treatment condition

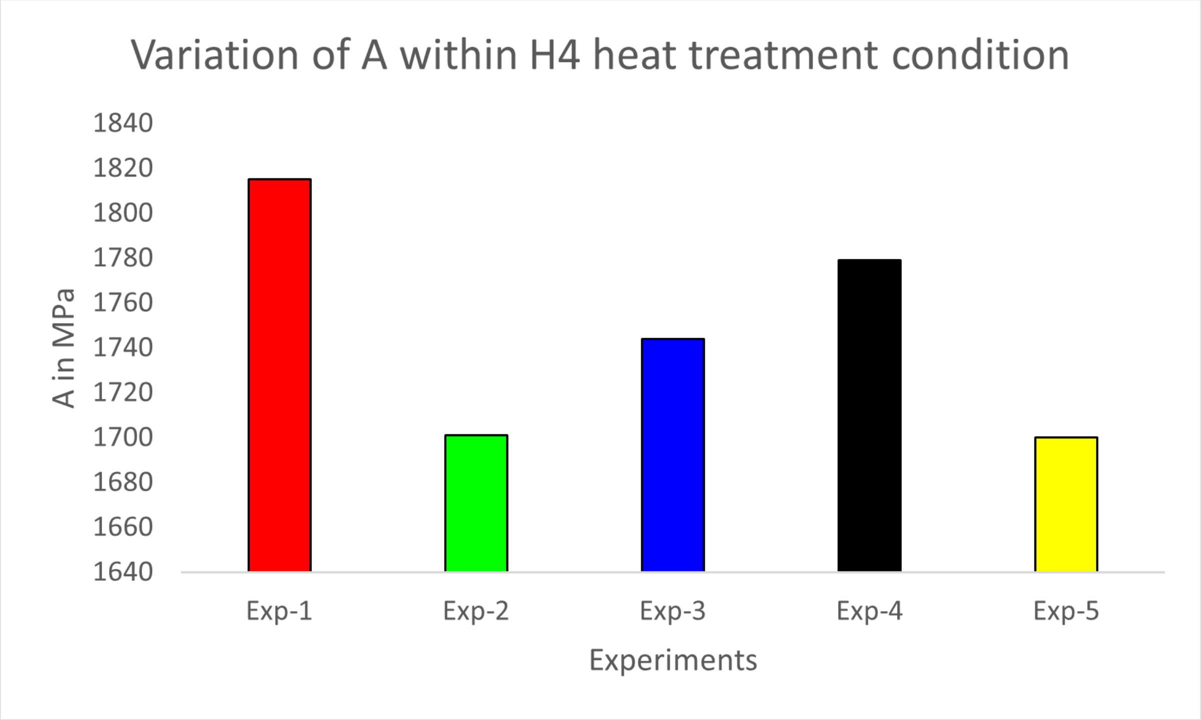

Figure 5.6: Variation of Yield strength for H4 heat treatment condition

the heat treatment conditions. Precipitates enhance the properties of the material. Figure 5.3

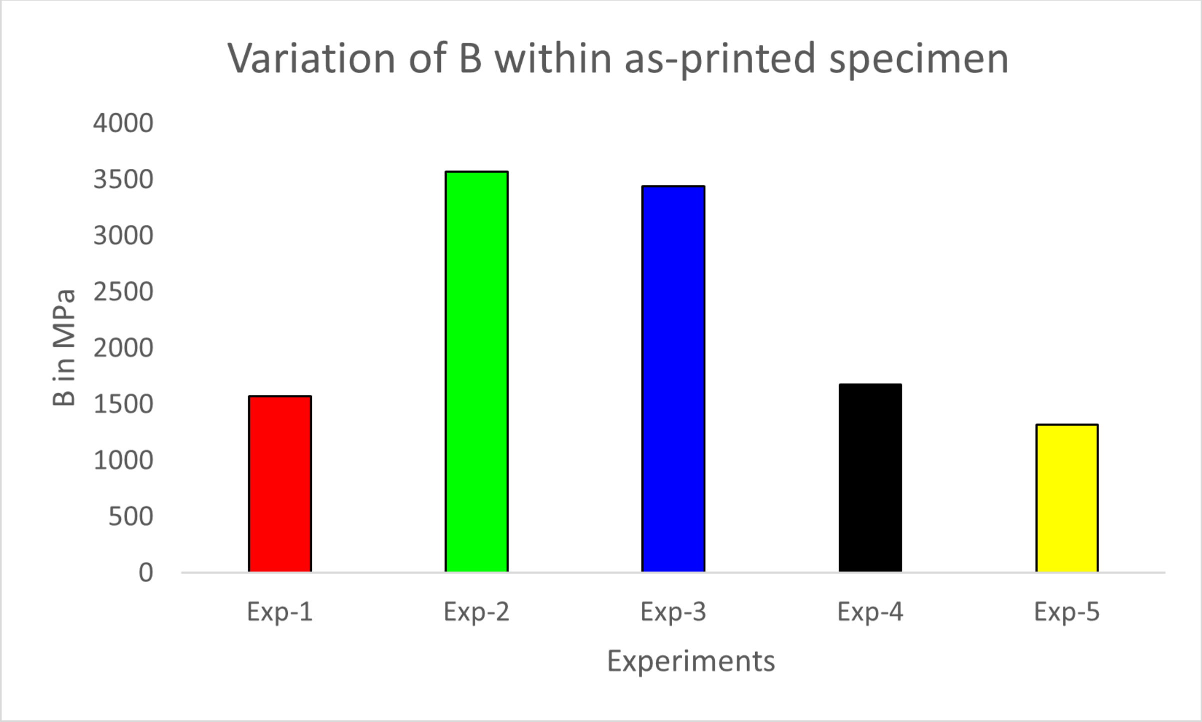

Figure 5.7: Variation of Strain hardening modulus for As-printed condition

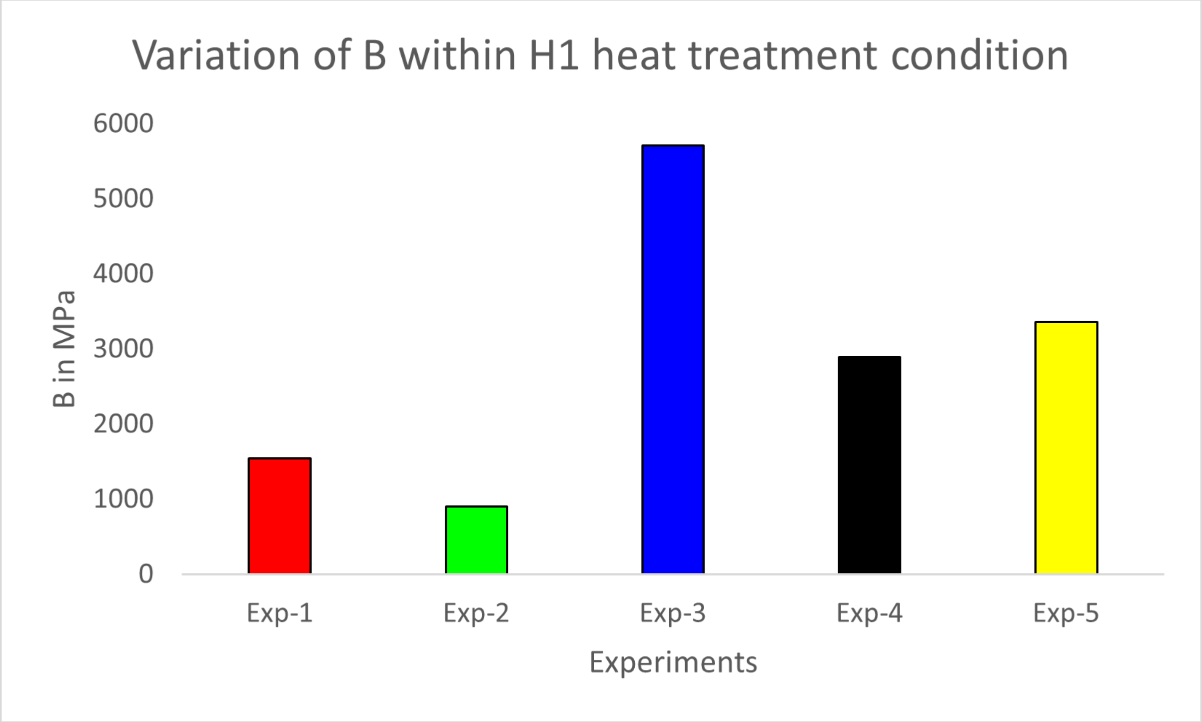

Figure 5.8: Variation of Strain hardening modulus for H1 heat treatment condition

portrays the variation of yield strength for H1 heat treatment condition. There was a disconnection of the strain gauge during the first experiment which was the main reason for a very high

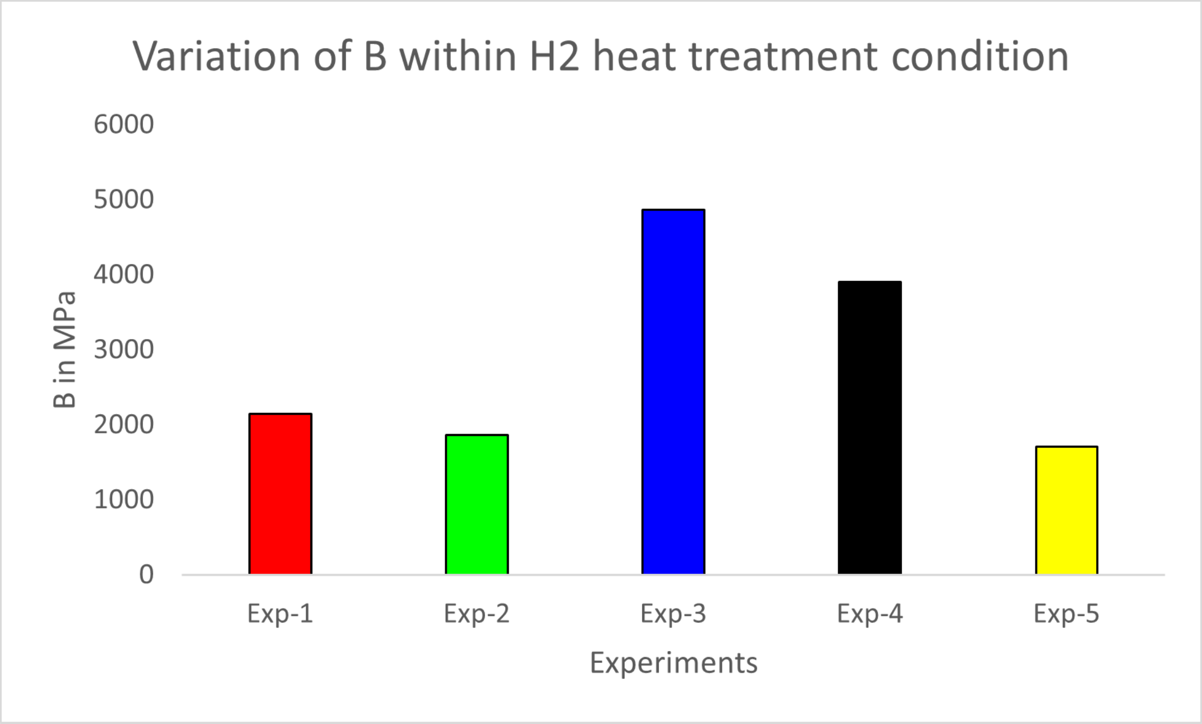

Figure 5.9: Variation of Strain hardening modulus for H2 heat treatment condition

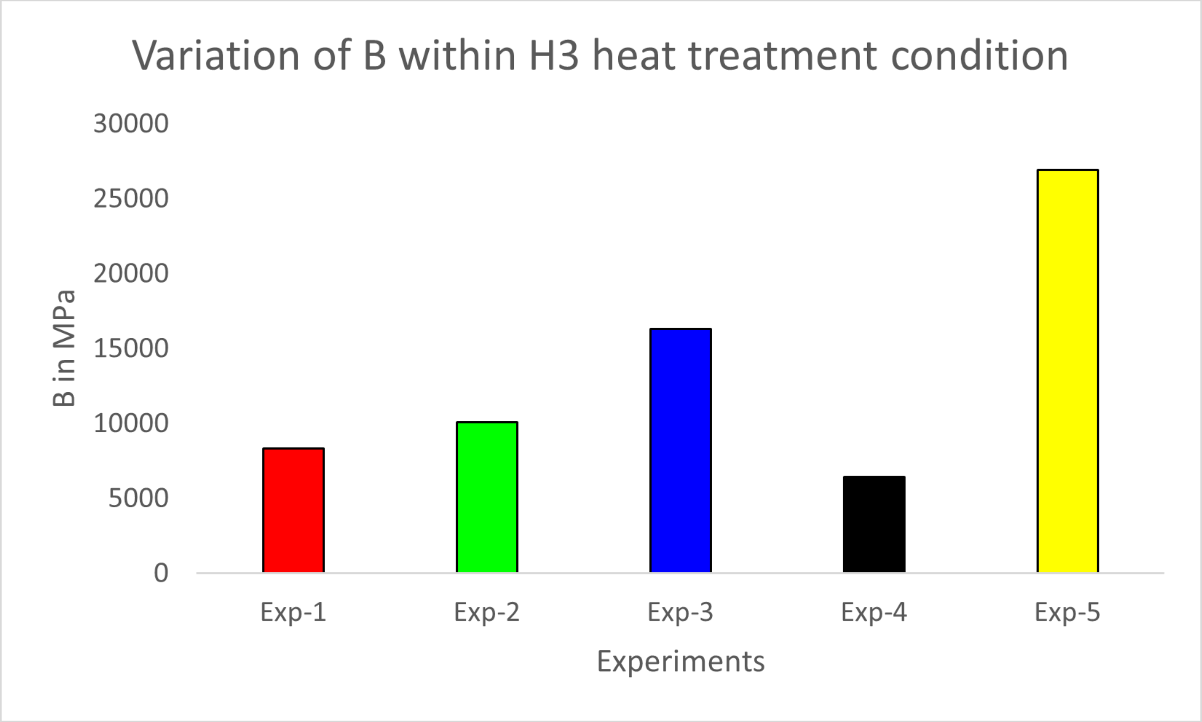

Figure 5.10: Variation of Strain hardening modulus for H3 heat treatment condition

variation in the yield strength of the specimen compared to the other counterparts of the H1 heat treatment condition. But with an increase in heat treatment, yield strength increases. [24]

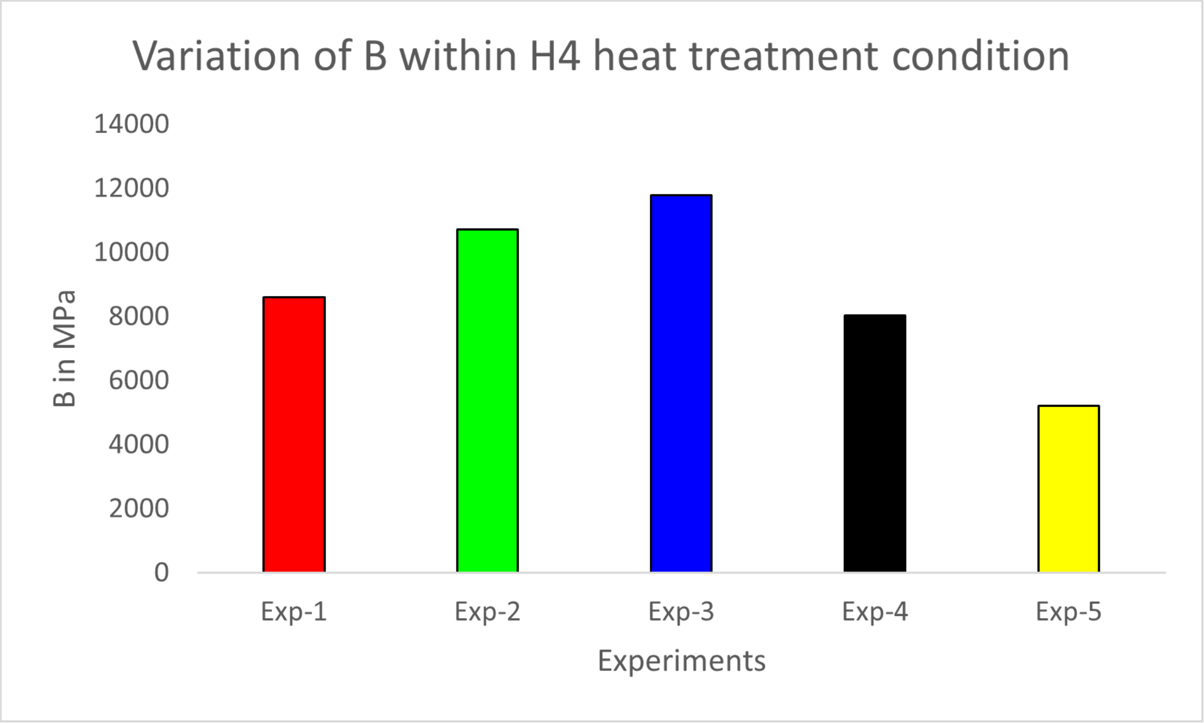

Figure 5.11: Variation of Strain hardening modulus for H4 heat treatment condition

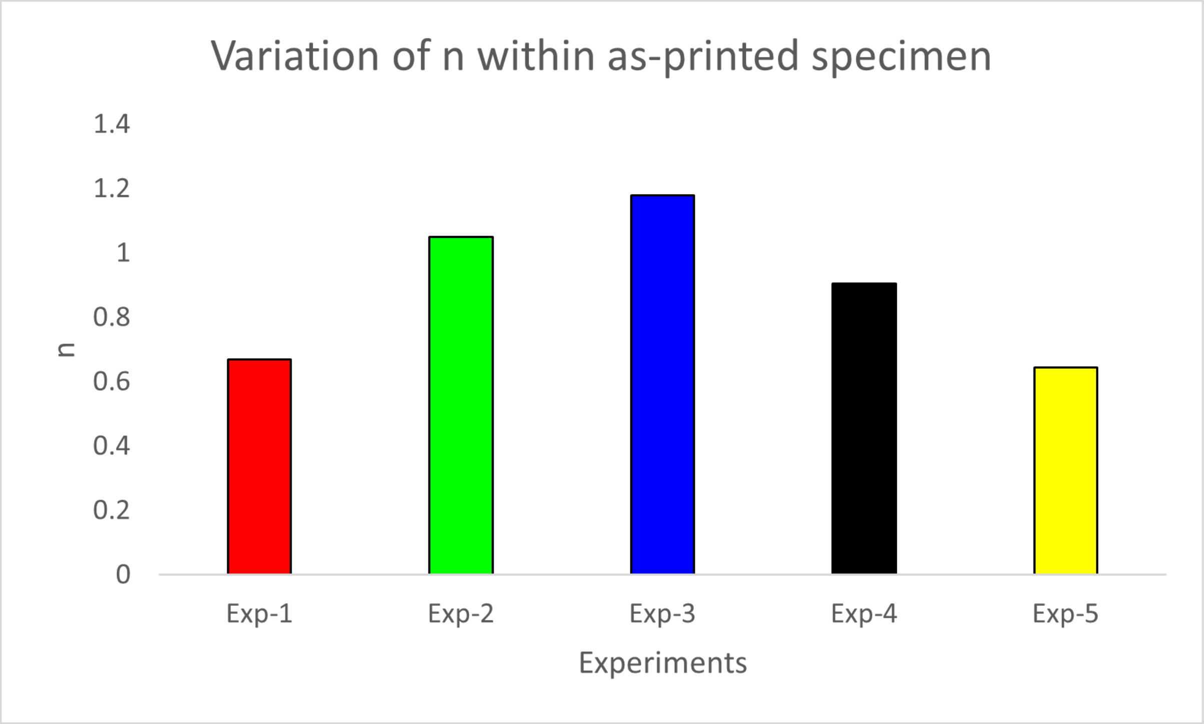

Figure 5.12: Variation of Strain hardening exponent for As-printed condition

states that, at H3 heat treatment conditions, maximum mechanical properties were obtained due to the formation of nanoscale Cu-rich spherical precipitates. This statement was proven

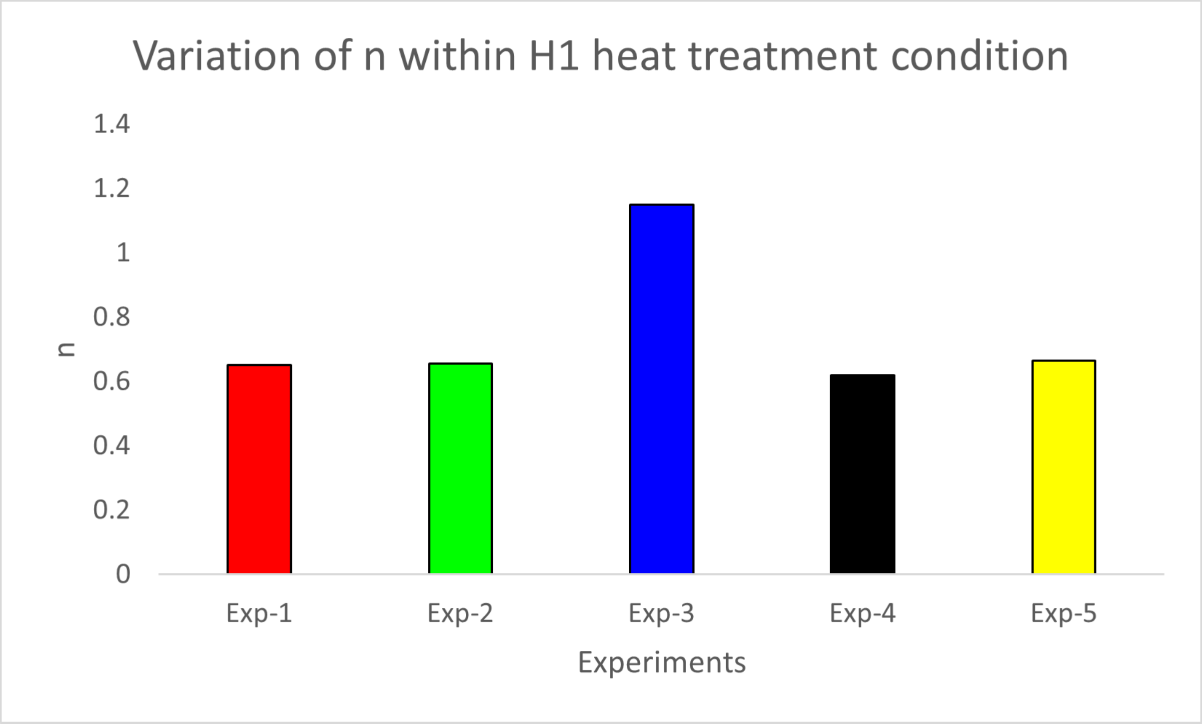

Figure 5.13: Variation of Strain hardening exponent for H1 heat treatment condition

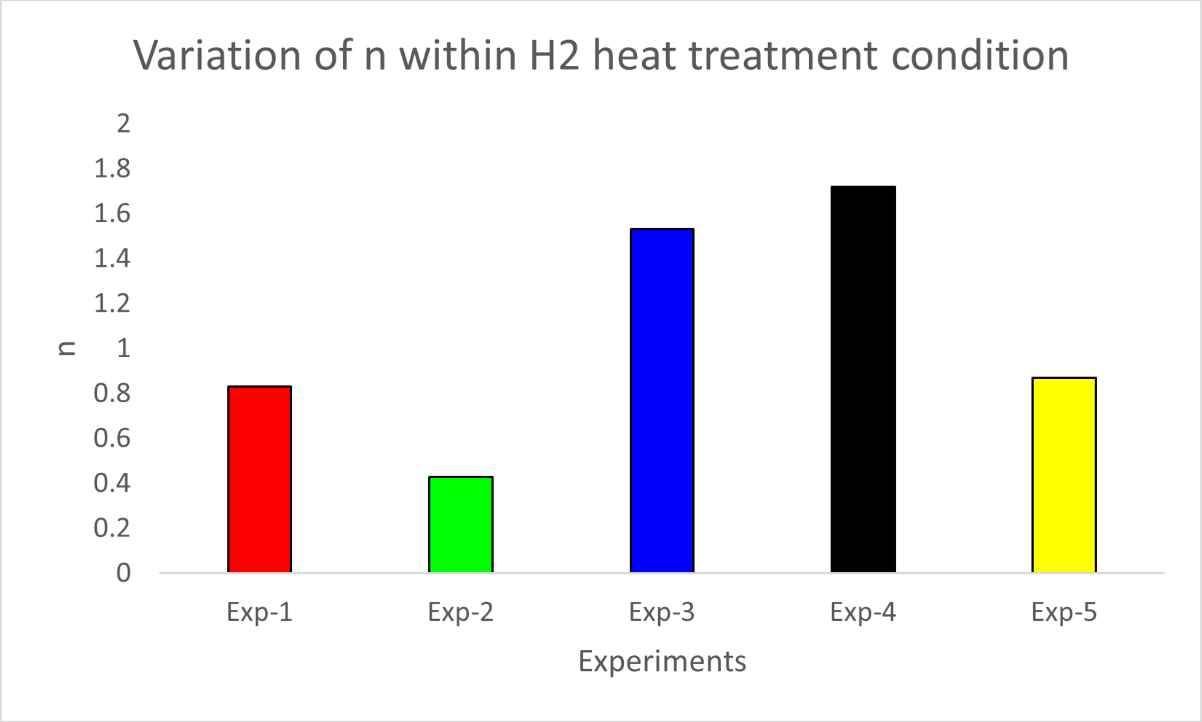

Figure 5.14: Variation of Strain hardening exponent for H2 heat treatment condition

correct as we observed maximum yield strength at H3 heat treatment condition. The same trend of increase in strain hardening modulus was observed with an increase in heat treatment

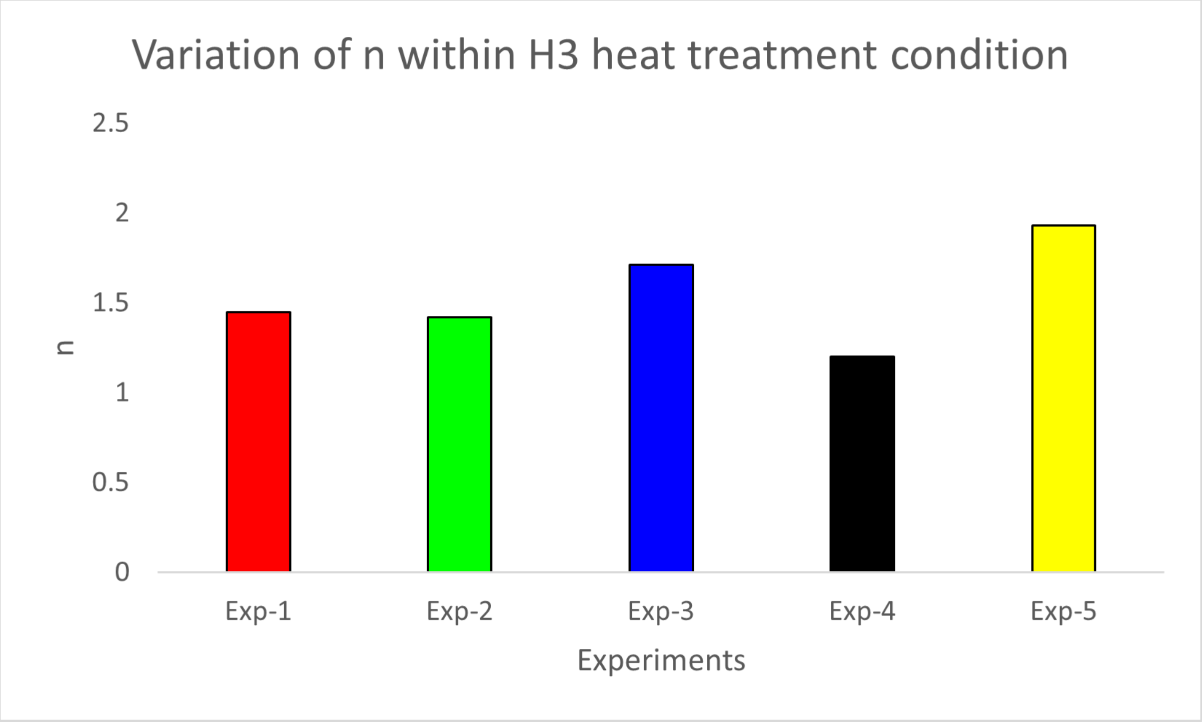

Figure 5.15: Variation of Strain hardening exponent for H3 heat treatment condition

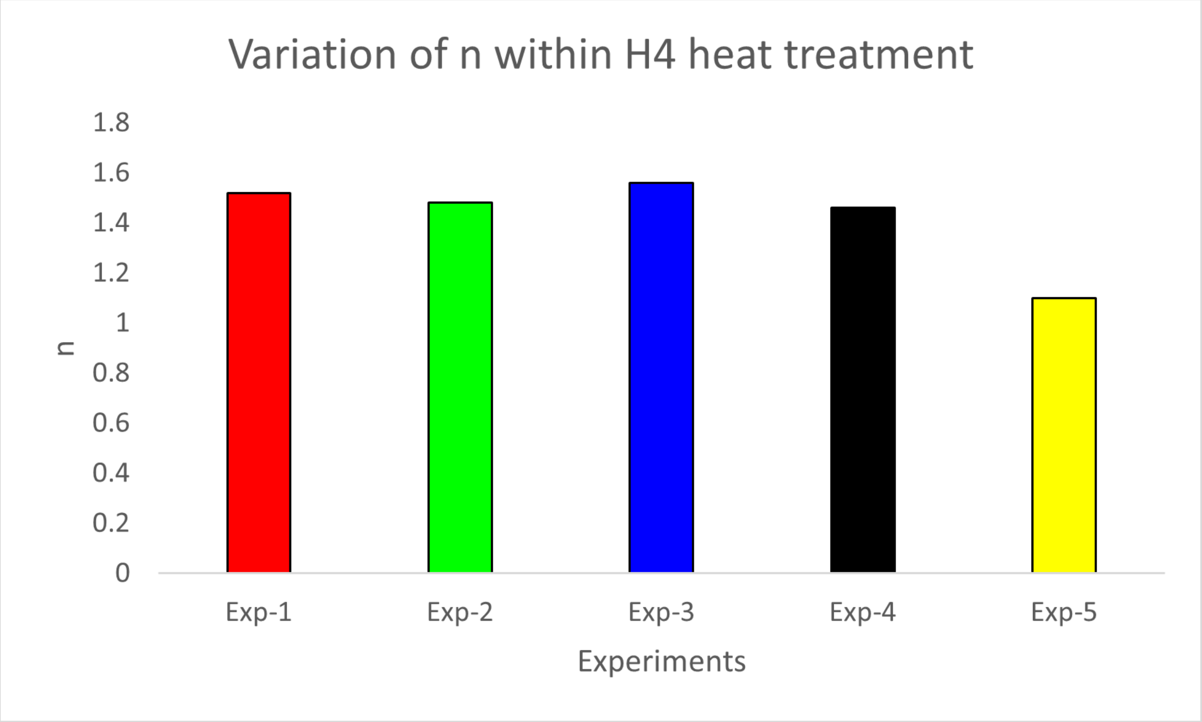

Figure 5.16: Variation of Strain hardening exponent for H4 heat treatment condition

conditions. Figure 5.7- Figure 5.11 represents the variation of strain hardening modulus for varying heat treatment. There were variations observed in the strain hardening modulus within the experiments at each heat treatment condition. The variation within each experiment can be justified by plotting the strain hardening rate to justify the variation within the experiments. The variation of strain hardening exponents within the experiments can be reasoned out with the help of a double logarithm plot.

Table 5.2: JC and Heat treatment parameters

Heat treatment case	A (MPa)	B (MPa)	n
NH	951.756±39.92	2314.27±39.92	0.89±0.23
H1	1190.4±39.92	2880.56±1868.5	0.75±0.22
H2	1263.6±116.17	2898.22±1407.7	1.075±0.53
H3	2012±37.68	13620±8298.6	1.54±0.28
H4	1747±47.94	8871.34±2553.17	1.42±0.18

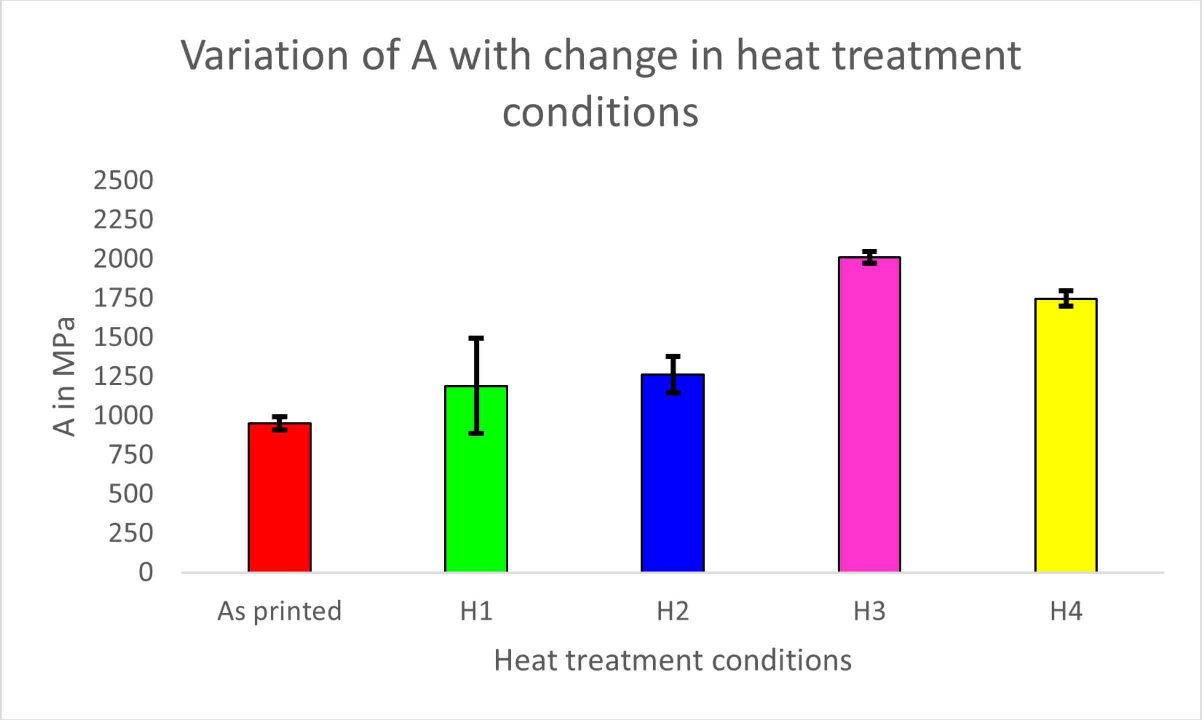

Figure 5.17: Variation of yield strength with error

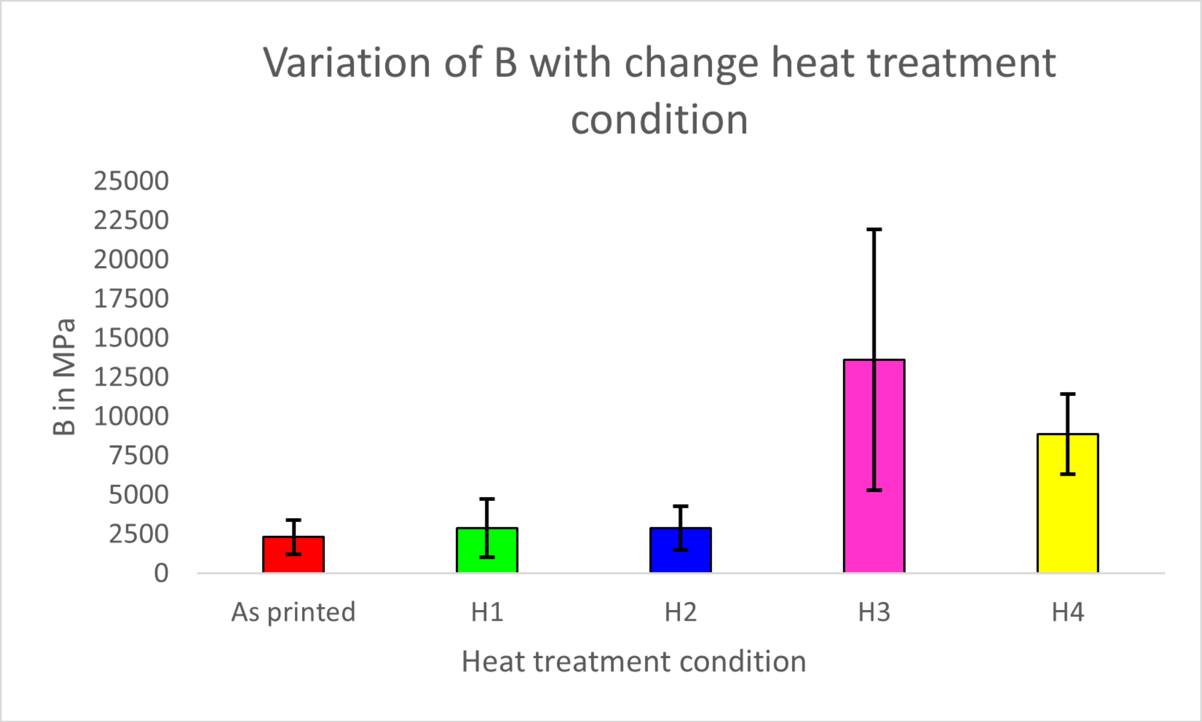

Figure 5.18: Variation of strain hardening modulus with error

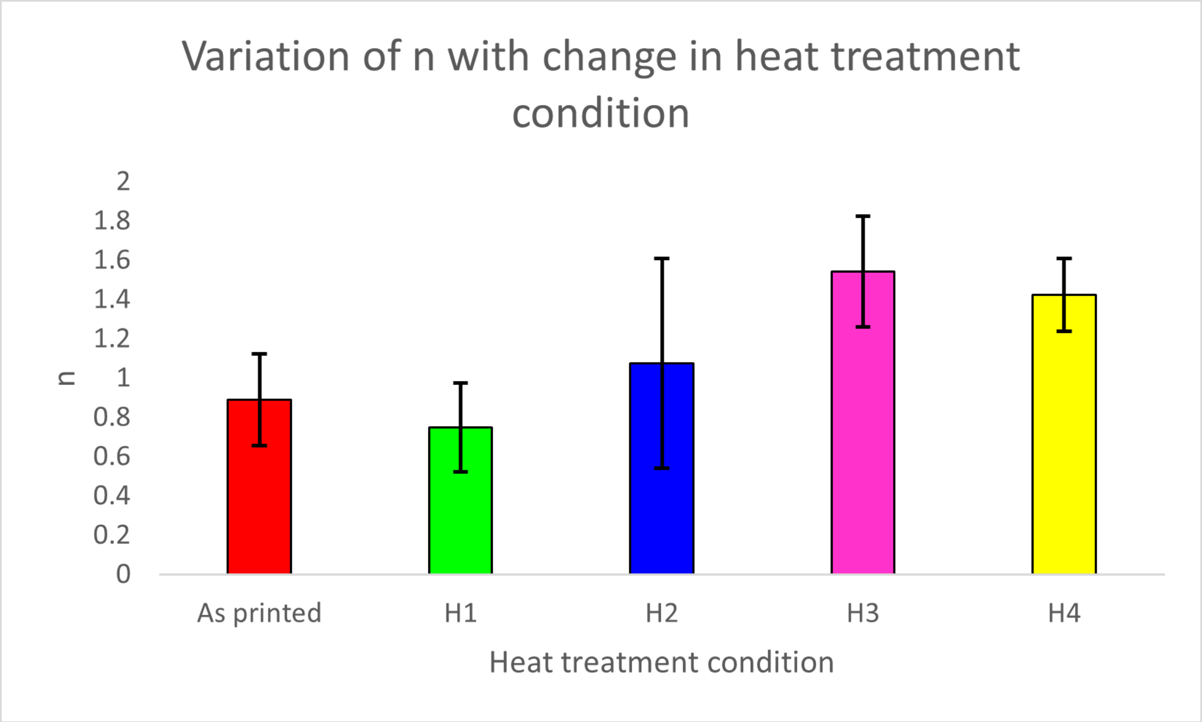

Figure 5.19: Variation of strain hardening exponent with error

5.1.2 Microstructure evolution

For observing the microstructure, grain size, and grain orientation before and after quasi-static and dynamic compression, the specimens are cut and mounted on conductive bakelite and polished using 9μm and 3μm diamond paste, and the mirror finish polish is done using OPS solution. After every step of polish, the specimens were immersed in a sonicator bath for about 15 minutes and exerted vibratory polish to remove the residual stresses during the polish and to improve the surface quality of the polished surfaces. Vibratory polish is usually done in a colloidal silica medium. After removing the vibratory polish, the specimen is placed in a sonnicator removing the colloidal silica particles, drying them, and placing them in a vacuum chamber for Scanning electron microscopy and electron backscattering diffraction tests.

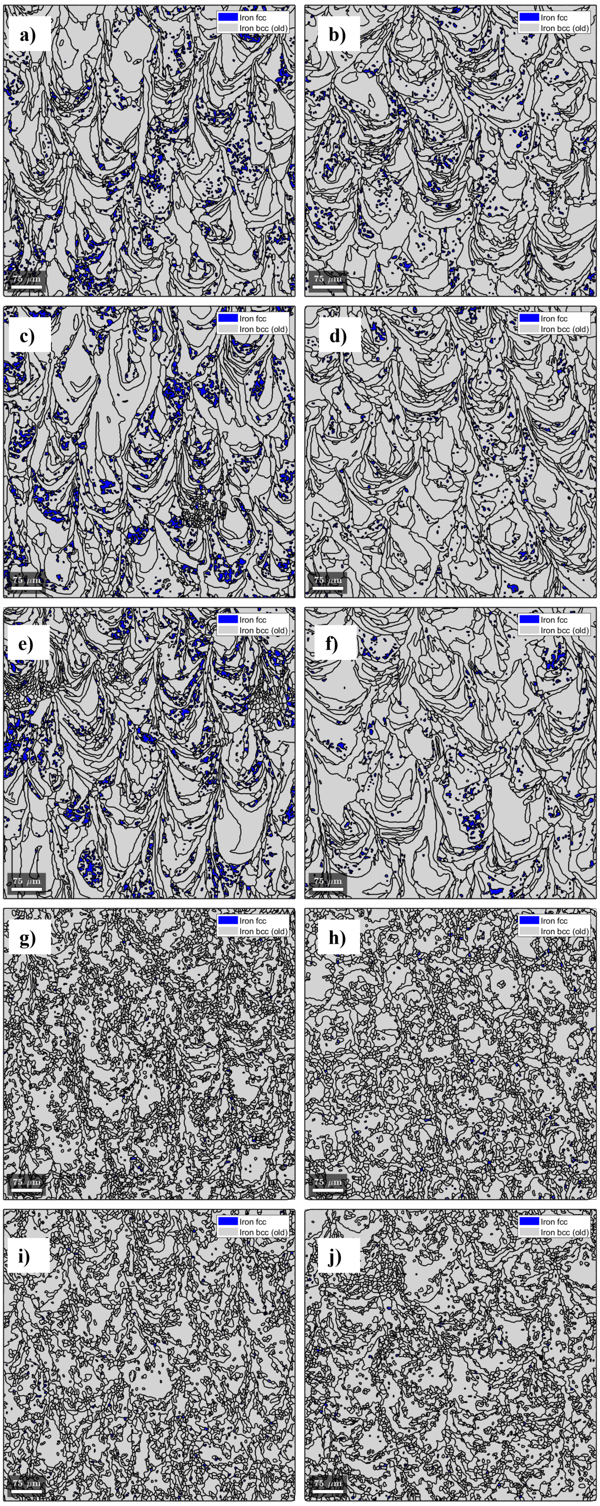

Figure 5.20: Phase plot for a)As printed condition b) H1 Heat treatment c)H2 Heat treatment d)H3 Heat treatment e)H4 Heat treatment

Figure 5.20 - Figure 5.23 describes the output from EBSD analysis namely phase plot, orientation plot, kernel average misorientation, and inverse pole figure. In the laser powder

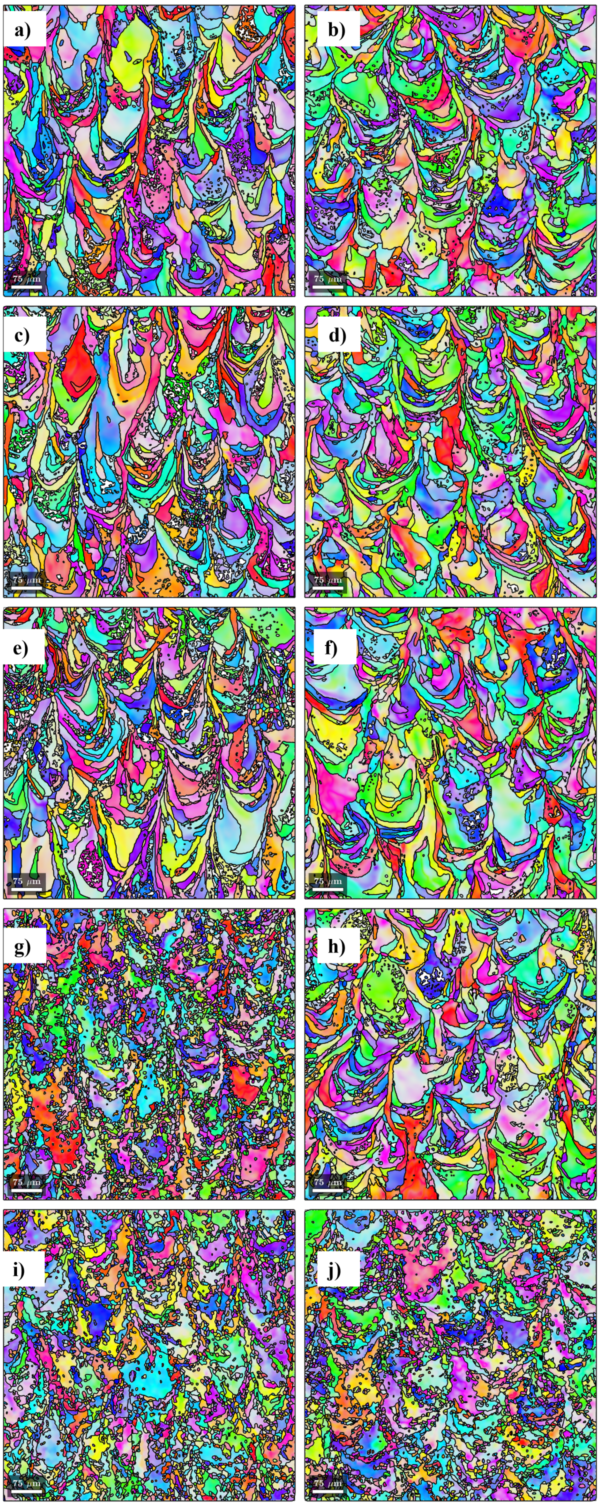

Figure 5.21: Orientation plot for a)-b)As printed condition pre and post-impact c)-d) H1 Heat treatment pre and post-impact e)-f)H2 Heat treatment pre and post-impact g)-h) H3 Heat treatment pre and post-impact i)- j)H4 Heat treatment pre and post-impact

bed fusion (LPBF) process, the formation of heterostructure grains, characterized by alternating coarser and finer grains, introduces a unique microstructural feature to the material. This

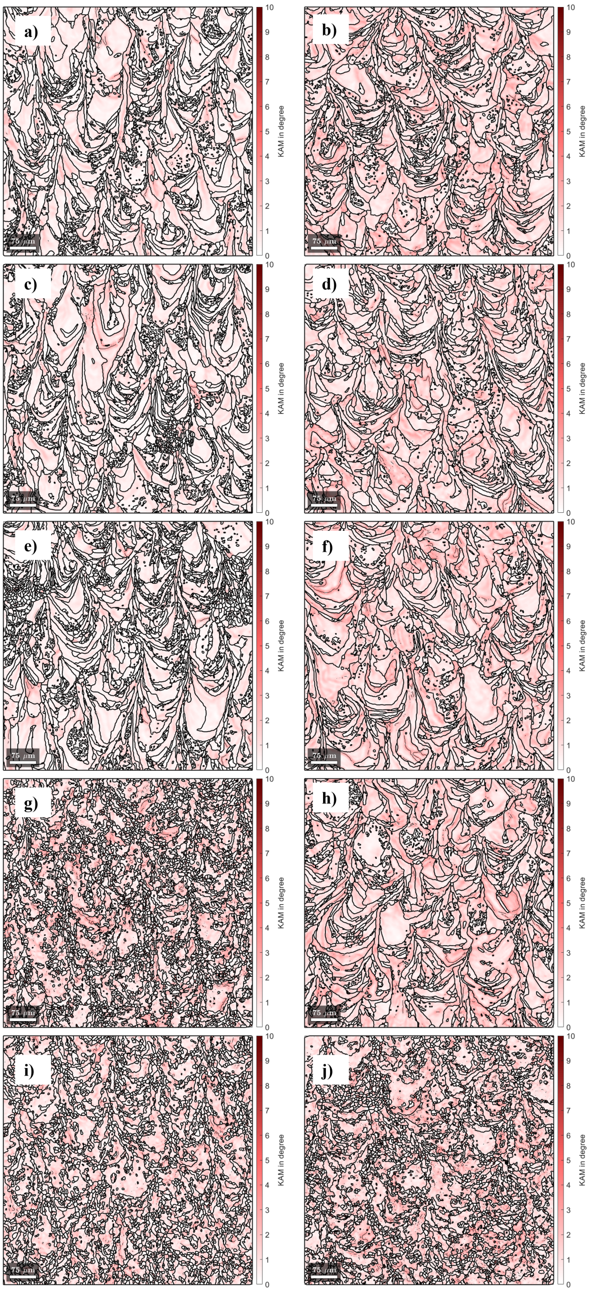

Figure 5.22: KAM for for a)-b)As printed condition pre and post-impact c)-d) H1 Heat treatment pre and post-impact e)-f)H2 Heat treatment pre and post-impact g)-h) H3 Heat treatment pre and post-impact i)- j)H4 Heat treatment pre and post-impact

heterogeneity plays a crucial role in influencing the mechanical properties of the final product. The alternation between columnar and equiaxed grains is a distinctive characteristic of heterostructure grains in LPBF. Coarser grains, often appearing columnar, contribute to enhanced ductility. Their elongated morphology provides a pathway for plastic deformation, improving the material's ability to undergo substantial strain without failure. On the other hand, the fine

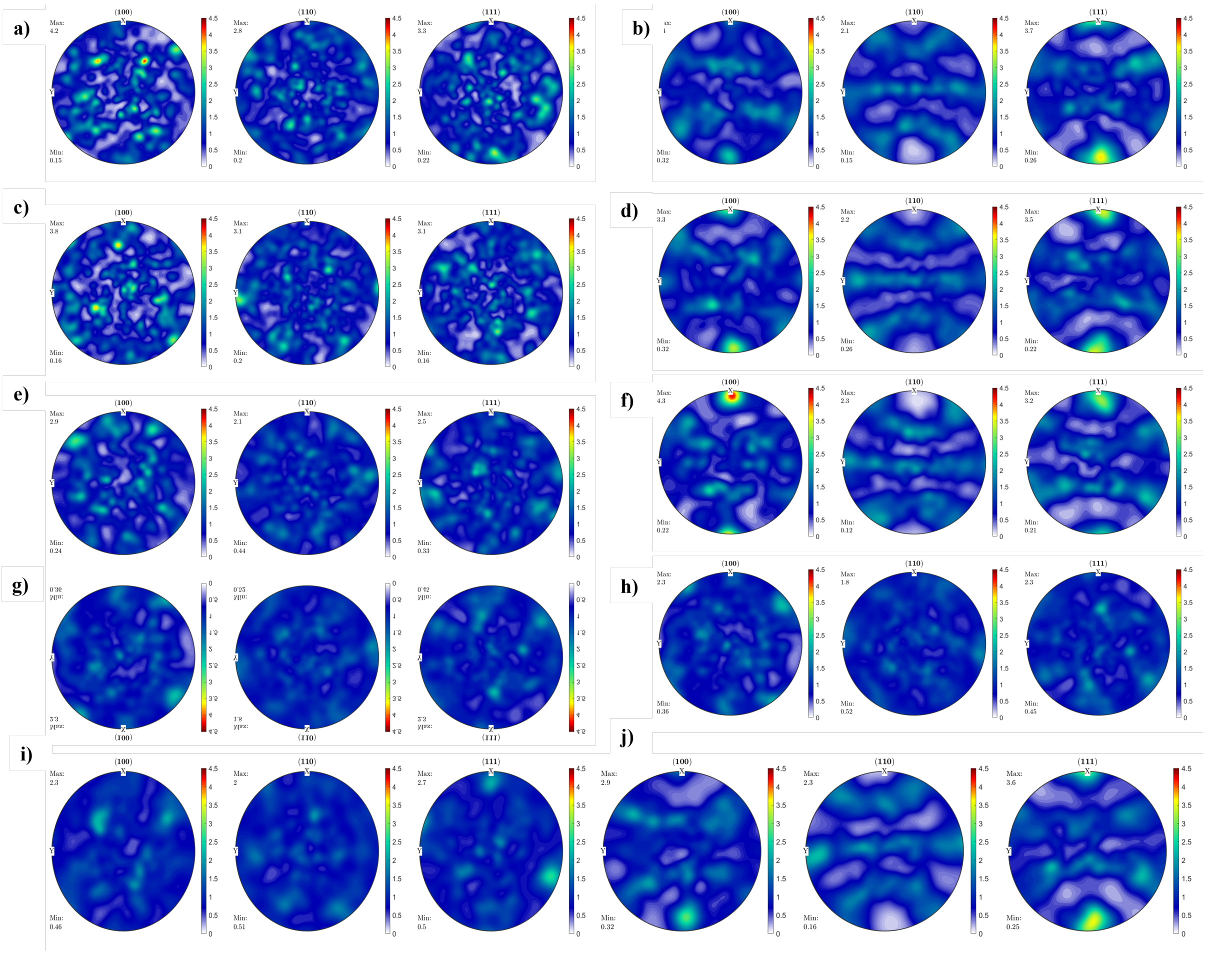

Figure 5.23: Inverse pole figure for for a)-b)As printed condition pre and post-impact c)-d) H1 Heat treatment pre and post-impact e)-f)H2 Heat treatment pre and post-impact g)-h) H3 Heat treatment pre and post-impact i)- j)H4 Heat treatment pre and post-impact

equiaxed grains interspersed between the coarser ones play a pivotal role in enhancing mechanical properties. Fine grains are associated with increased strength and hardness, contributing to improved wear resistance and structural integrity. Their smaller size allows for a higher density of grain boundaries, which can impede dislocation movement and enhance the material's resistance to deformation. Phase plots and orientation plots serve as invaluable tools for visualizing and analyzing the intricate details of these microstructures. This article delves into the significance of phase plots and orientation plots, with a specific focus on their application in studying the heat treatment of 17-4 steel. In the case of 17-4 steel, a precipitation-hardening stainless steel alloy, phase plots become particularly informative during heat treatment. As the temperature and duration of heat treatment increase, the alloy changes its microstructure, including the dissolution of the face-centered cubic (FCC) phase. Phase plots allow researchers to track and quantify these transformations. The FCC phase in 17-4 steel plays a pivotal role in determining the alloy's mechanical properties. As heat treatment progresses, the phase plot becomes a dynamic canvas illustrating the dissolving of the FCC phase. Orientation plots take the analysis a step further by providing insights into the orientation of individual grains within the microstructure. These plots are particularly valuable for understanding the deformation and mechanical behavior of materials. In an orientation plot, each grain is represented by a specific color on an inverse pole figure (IPF) key. The color scale in the IPF key corresponds to different directions within the lattice structure of each grain. This means that a single grain may exhibit multiple colors, reflecting variations in its orientation resulting from deformation. For 17-4 steel, orientation plots become crucial in unraveling the complexities of the alloy's microstructure during heat treatment. Deformation-induced changes in the lattice structure are visually evident through the varying colors within individual grains. Researchers can use these plots to gain a nuanced understanding of how the alloy responds to thermal and mechanical treatments. The IPF key serves as a color triangle, allowing researchers to decode the orientation of grains based on the color spectrum. This enables the identification of areas with specific lattice orientations, contributing to a comprehensive analysis of the microstructural landscape. To gain a holistic perspective on the evolution of 17-4 steel microstructures during heat treatment, combining phase and orientation analyses is paramount. The phase plot provides a macroscopic view, highlighting the distribution of different phases and their changes over time. On the other hand, orientation plots offer a microscopic lens, revealing the intricate details of individual grain orientations and their response to thermal and mechanical influences. In examining the microstructural changes induced by heat treatments 3 and 4, it becomes apparent that both treatments involve annealing/stress relief, possibly coupled with a precipitation-based hardening mechanism. Heat treatment 3, characterized by extended time and temperature, appears to have a profound impact on the microstructure. The recrystallization process is notably pronounced, indicating a substantial transformation in the material. Moving to heat treatment 4, the similarities with heat treatment 3 are evident, yet there is a distinct feature of grain growth. The presence of larger grains in heat treatment 4 suggests that, in addition to the annealing and stress relief, the microstructure has undergone a process of grain coarsening or growth. Grain growth is a phenomenon where smaller grains fuse or consume neighboring grains, resulting in the formation of larger grains. The occurrence of grain growth in heat treatment 4 implies that the material experienced an extended period at an elevated temperature, allowing for the mobility of atoms and the coalescence of grains. This prolonged exposure to heat facilitates the rearrangement of atoms along grain boundaries, leading to the observed enlargement of grains. The growth in grain size can have significant implications for the material's mechanical properties, such as changes in strength, hardness, and possibly grain boundary characteristics. It's important to note that the specific characteristics of the grain growth, such as the rate and extent, would require detailed information on the time-temperature profile and, ideally, a Time-Temperature-Transformation (TTT) diagram for the alloy in question. Additionally, the identification of any precipitation-based hardening mechanisms should be confirmed through a comprehensive analysis, including examination of relevant alloy phase diagrams and precipitation kinetics. In summary, while heat treatments 3 and 4 share similarities in terms of annealing/stress relief and potential hardening mechanisms, the distinguishing factor in heat treatment 4 is the presence of observable grain growth. This phenomenon indicates a more prolonged exposure to elevated temperatures, resulting in the coalescence and enlargement of grains within the microstructure. Understanding these nuanced changes is crucial for tailoring the material's properties to meet specific performance requirements.

Chapter 6

Results for Fused Filament Fabrication

6.1 Quasi-static and Dynamic compressive behavior of Fused Filament Fabrication samples

17-4 PH stainless steel fabricated using a fused filament fabrication route is cut into the required specimen using an electric discharge machining process. It was ensured that the specimens were cut along the print direction so that the quasi-static and dynamic compression test could happen along the print direction. As this process induces porosity during manufacturing the specimen had to be examined for porosity under macro X-Ray CT. Figure 6.1 describes the porosity scan for a green sample. The as-printed block is cut using a band saw for the dimension of 5mm x 5 mm x 10 mm and placed in the XCT chamber between the x-ray source and the detector. From the scan, it is observed that the green part is still soft and yet to attain rigidity. The print happens in a layer-by-layer fashion which gives rise to porosity. During the process of sintering, when placed inside a furnace, the polymer in the polymer/metal hybrid green part evaporates and shrinks the rest of the 17-4 PH stainless steel particles present in the green part reducing the dimensions of the printed part. The end product is a 17-4 PH stainless steel component. It is also observed that the large pores and gaps are filled during the process of sintering reducing the overall diameter of the porosity. Figure 6.2 gives a brief statistical distribution of the equivalent pore diameter of the green sample. This states that the majority of the pore diameter lies between 20 μm - 120μm which is proven by the porosity analysis through XCT. The $\%$ porosity in a green sample which was observed was approximately about 7$\%$. But after sintering the green part there was a 2$\%$ reduction in porosity approximately. The bigger pores started breaking down into smaller pores which is shown in figure 5.14. The

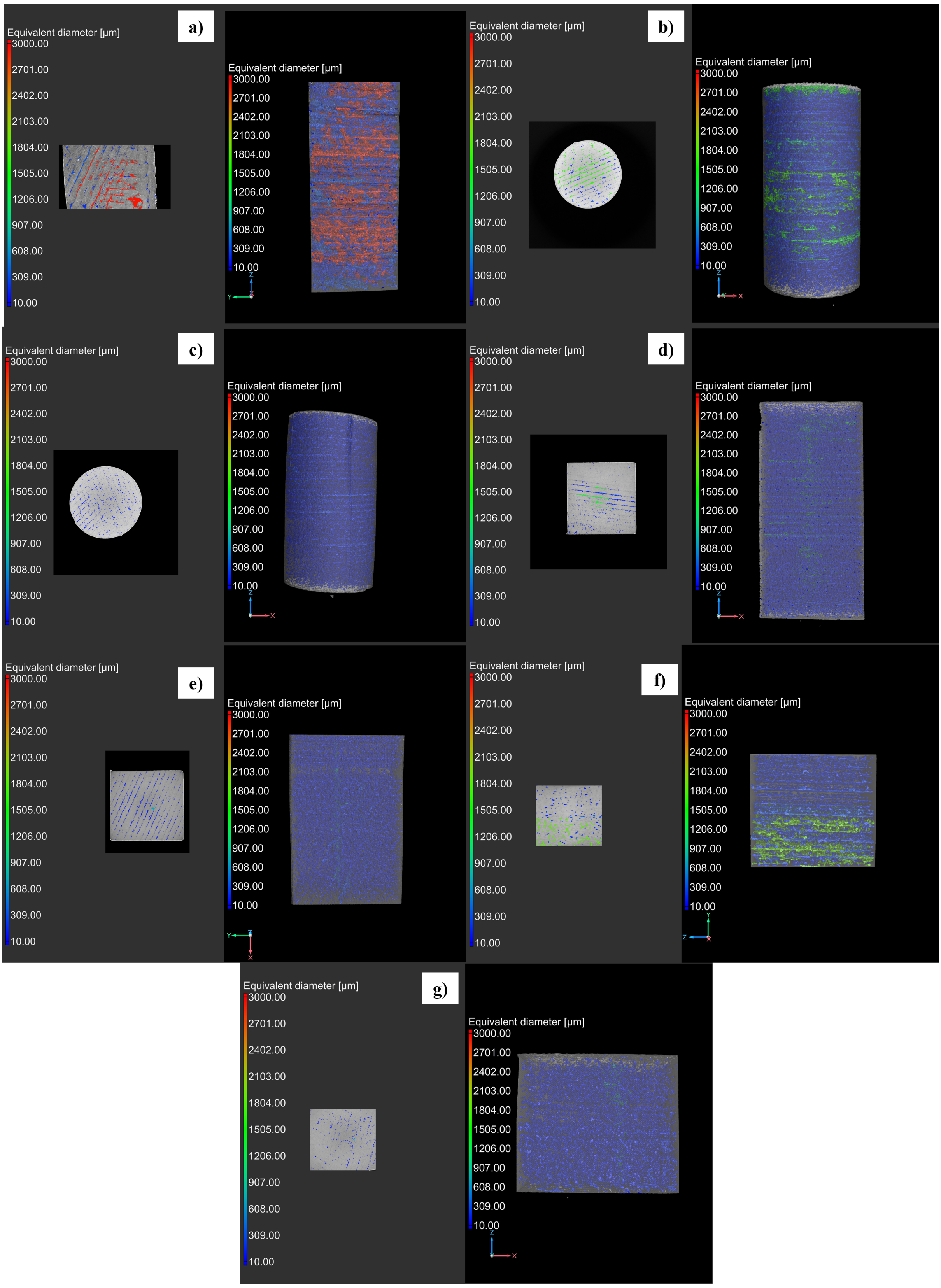

Figure 6.1: X-Ray CT images of green, sintered, and impacted samples

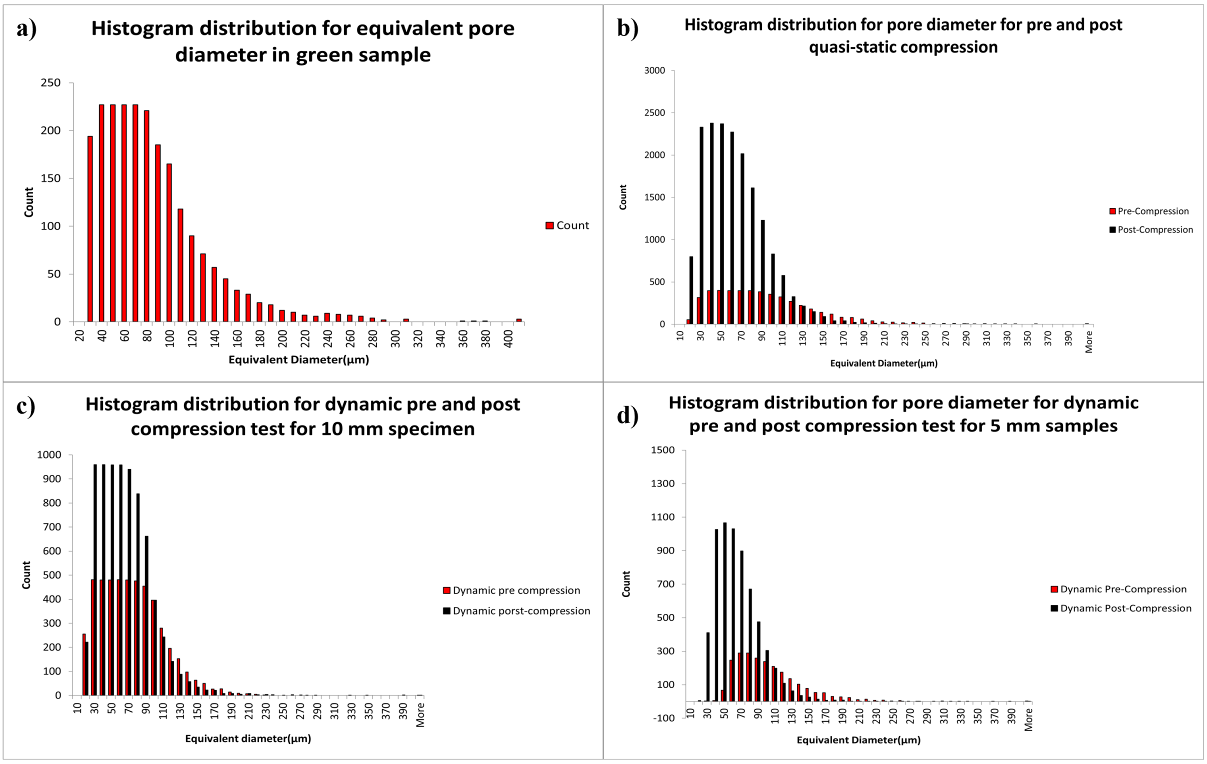

Figure 6.2: Histogram distribution for green, sintered, and impacted samples

count of pores between the equivalent diameter of 20 μm - 120μm increased after the sintering process. When exerted to a compression process, there occurs a collapse of pores which works right opposite to the principle during a tension process where a small pore grows into a bigger size pore creating the core region for failure. That principle is observed both in quasi-static and dynamic compression tests. As quasi-static compression occurs at the strain rate of 10^{-3} s^{-1}, the experiment practically occurs at a very slow rate, so the time required for all the pores to react is high. So the reduction in pore diameter in the 20 μm - 120μm range is twice that of occurring at a dynamic compression test which is shown in figure 5.14. Figure 5.15 and 5.16 describes the statistical distribution of pores before and after the dynamic compression test at a strain rate of $625s^{-1}$ and $1250s^{-1}$. There is a slight variation between the porosity count before impact for samples cut for quasi-static compression and dynamic compression. The reason for the slight variation is due to the region from which the specimens were cut for respective quasi-static and dynamic compression tests which is a key factor in having uniform porosity distribution. During the dynamic compression test, the experiment is so quick that the pore interaction time is minimal. A similar reduction in pores between 20 μm - 120μm range

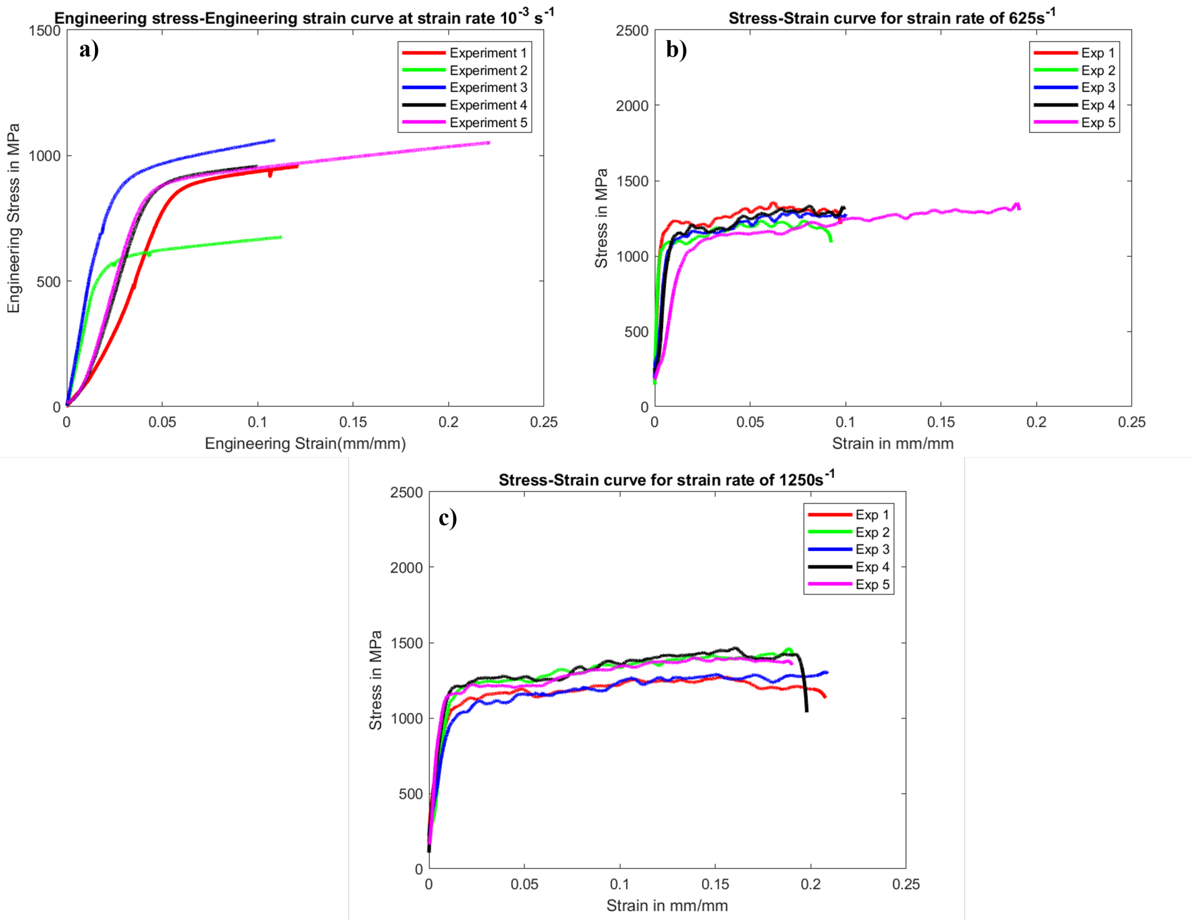

Figure 6.3: Quasi-static and Dynamic stress-strain curve

is observed but the count of pores in that region is smaller. It's half that of the occurrence of that from the quasi-static compression test. Figure 5.17 describes the engineering stress-engineering strain curve for a quasi-static compression test occurring at a strain rate of 10^{-3} s^{-1}. The specimen of diameter 5 mm and length 10 mm is placed between two parallel plates in the INSTRON 5310 machine with a load cell capacity of 100kN. When the load is applied the material slowly starts deforming taking the load. The porosity between the layers started to interact with each other, bigger pores started to collapse into tiny pores. The experiment was stopped when the specimen started deforming without taking the load. The data we obtain from the quasi-static compression test is load vs displacement data which needs to be converted to stress vs strain data. With the area of cross-section and length of the specimen being known stress vs strain can be calculated. Figure 5.17 depicts the quasi-static stress-strain curve. Five experiments were conducted to ensure repeatability. There was a difference in the slope of the stress-strain curve due to the presence of porosity and the location from which the specimen was cut. The compression was ensured to occur along the print direction. But we do need to focus on the true stress-true strain data which requires conversion of engineering stress-engineering strain data to true stress-true strain data. The engineering stress-engineering strain data is converted using the equations 7 and 8.

$$\epsilon_{True} = ln(1 + \epsilon_{engg}) \tag{6.1}$$

$$\sigma_{True} = \sigma_{engg}(1 + \epsilon_{engg}) \tag{6.2}$$

The yield strength of additively manufactured 17-4 PH stainless steel through fused filament fabrication is calculated using the 0.2% offset method. A parallel line with the same slope as the elastic region is plotted and the intersection between the stress-strain curve and the parallel line fetches us the yield strength. Figure 6.4 describes the variation of yield strength between

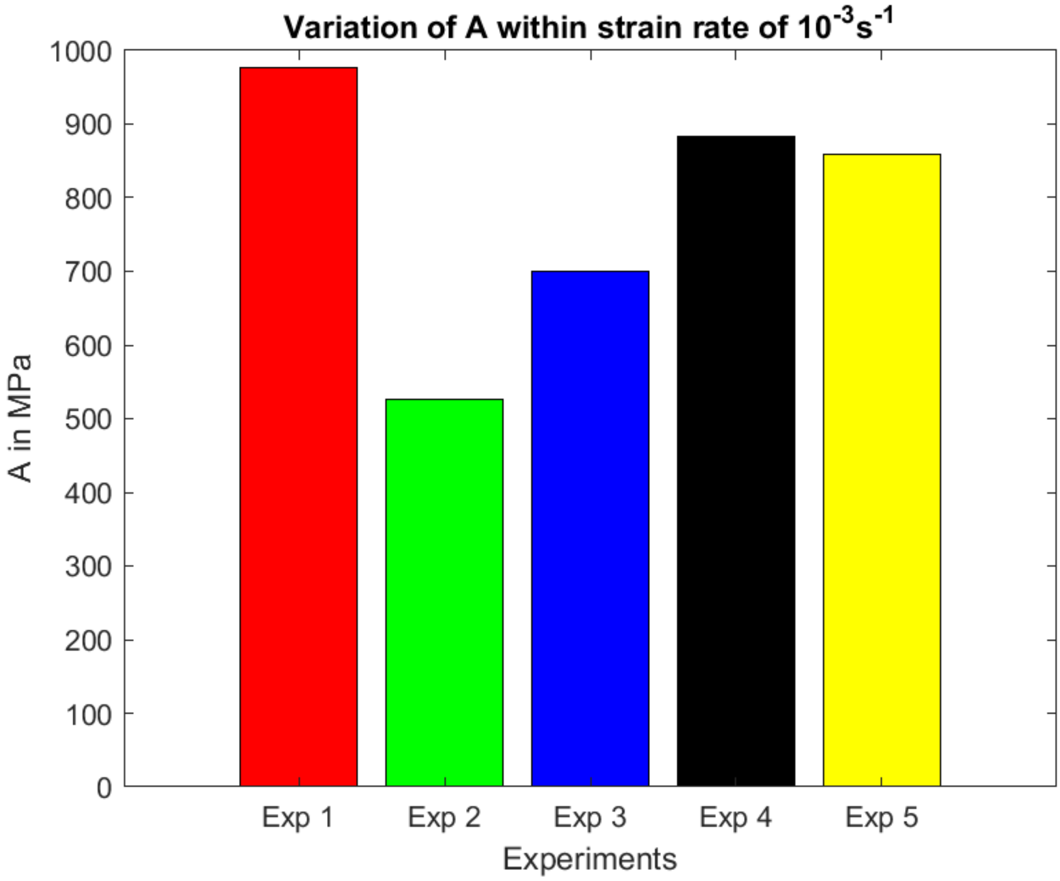

Figure 6.4: Variation of yield strength within the quasi-static compression test

the experiments in a quasi-static compression test. The variation in yield strength is observed from the stress-strain curve with varying slopes in the elastic region and the reason for such a variation is because of location and the position of porosity. In a couple of experiments, there was a jump in the stress-strain curve after the elastic region. The reason for the jump can be expected to be layer-to-layer interaction between porosities which causes a slight vertical variation. The average yield strength is about 788 ± 176.88 MPa. The difference in standard deviation is because of porosity, and location from where the specimen was cut. Figure 6.5 depicts the dynamic response of 17-4 PH stainless steel. The experiments occur at two different strain rates of 625 $^{-1}$ and 1250 $^{-1}$. Two approaches can achieve a change in strain rate during the experiment. One is by changing the pressure and the other is by increasing or decreasing the length of the specimen. At a given value of pressure, a lower strain rate can be achieved by increasing the length of the specimen. But a few assumptions have to be taken care of which is the length of the specimen should not be larger than the diameter of the incident/transmission bar. So specimens of dimensions 5 mm x 5mm x 5mm and 5mm x 5mm x 10mm have been chosen for determining the dynamic response using the Kolsky compression bar. The strain signals from the strain gauge are recorded and converted into stress-strain data. Experiments were conducted at a pressure of 12.9 PSI for both specimens of length 5mm and 10mm respectively. With the increase in strain rate from 625 $^{-1}$ to 1250 $^{-1}$, there is an increase in yield strength of the material which is observed in Figure 5.8b and 5.8c from the dynamic stress-strain curve. For a monolithic material, it has been observed in the literature that with an increase in strain rate, the slope of the elastic region increases. But metals fabricated using fused filament fabrication process in their as-printed state are highly porous. The material in its printed condition falls between the category of fully dense material and lattice structure. So the behavior with varying strain rates is not explored to the fullest extent. In our case, we are experiencing a decrease in the slope of the elastic region with an increase in strain rate when viewed in a very close range. The material under both strain rates exhibits linear elastic behavior followed by strain hardening behavior with a significant influence on the effect of strain rate. With the increase in strain rate, there was an increase in the yield strength of the material. When strain rate of increased from 625 to $1250s^{-1}$ the yield strength increased by 9.35% from 1058 MPa

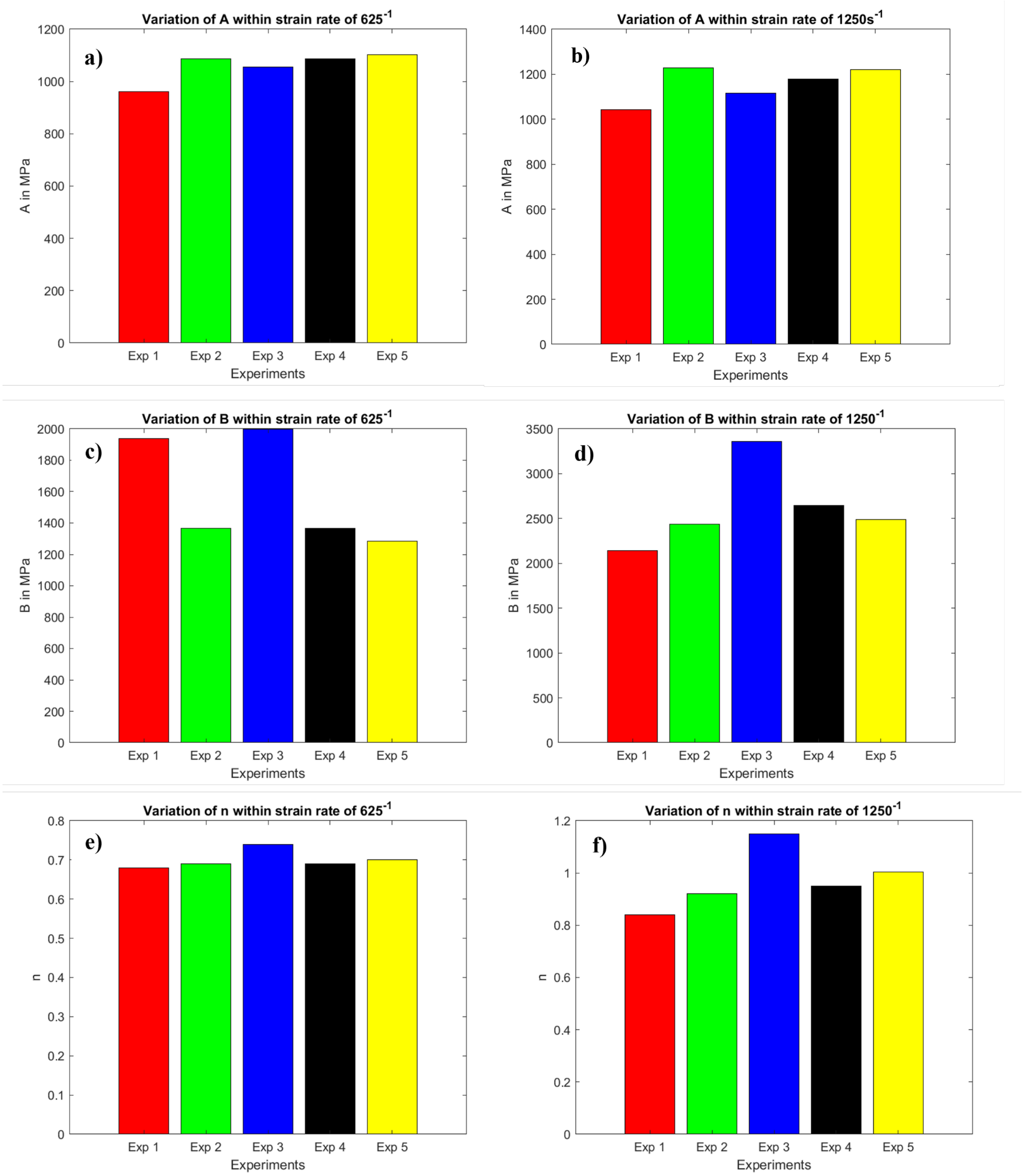

Figure 6.5: Yield strength, Strain Hardening Modulus, and Strain hardening exponent for dynamic compression test

to 1157 MPa. From quasi-static condition to a strain rate of $625s^{-1}$ there is an increase in yield strength by a magnitude of 34.6 $\%$ and 46.85$\%$ from quasi-static to $1250s^{-1}$. The main concern when working with porous samples was whether the dynamic response is because of the material microstructure or porosity which is influencing the stress-strain response. To ensure

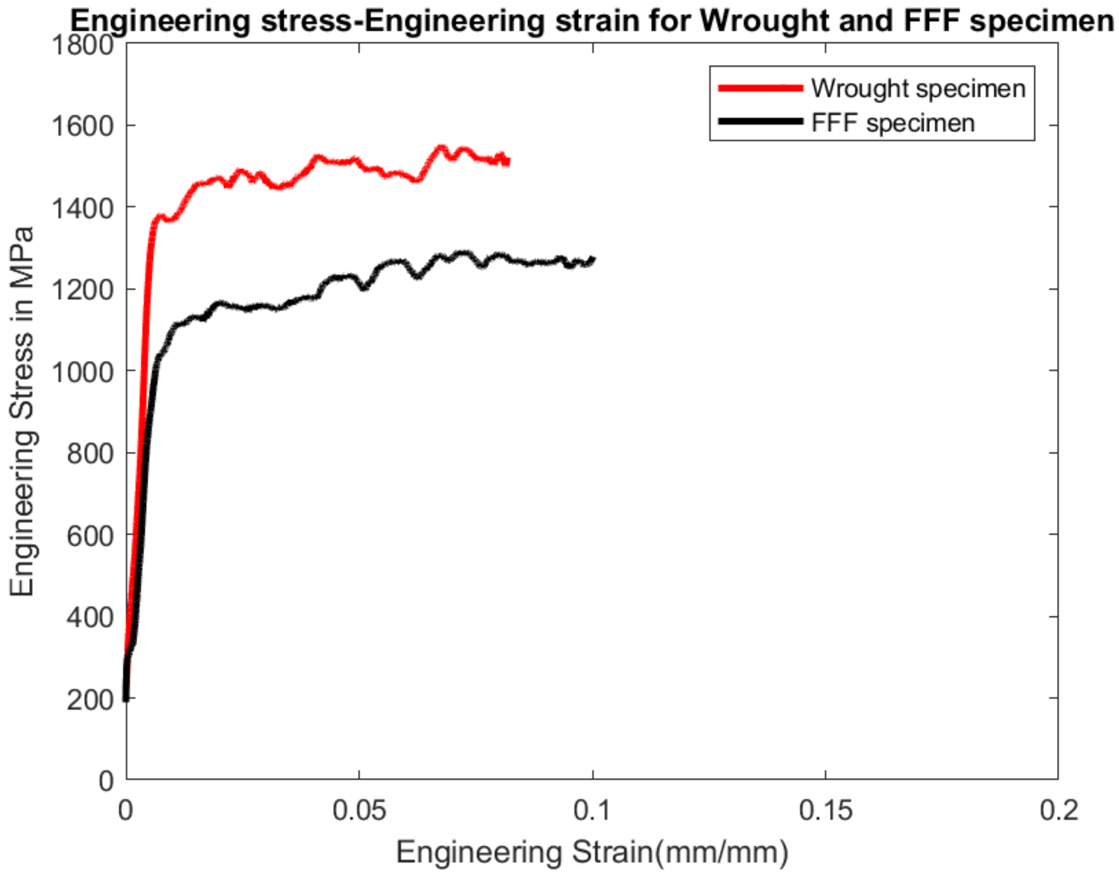

Figure 6.6: Stress-strain plot for Wrought specimen and FFF specimen at a strain rate of $625s^{-1}$

this question, a wrought sample which was commercially purchased was cut into dimensions of 5mm x 5 mm x 10 mm, and the pre-compressed sample was scanned in XCT to analyze the porosity in the sample. As the 17-4PH commercially acquired sample was forged, there was no porosity observed as it was completely dense. So the hypothesis was if the yield strength was equal to that of the yield strength obtained from the wrought sample, then the dynamic response if microstructure driven. If the yield strength obtained is less than that of the wrought specimen, then the dynamic response is influenced by porosity. In this case, there was a difference of 300MPa in yield strength between the wrought sample and the fused filament fabricated sample which is observed from figure 6.6 So this proves that porosity influences the dynamic response of an as-printed fused filament fabricated sample.

From the true stress-true strain curve, the next step is to extract the material constants for a Johnson-Cook model. The generic Johnson-Cook model is given in equation 4.1. For the case of Fused Filament Fabrication samples, temperature is maintained as a constant but there arises variation in strain rate. So the method of extraction is different in this case. So the extraction procedure for variation of strain rate is listed below. There are a few steps required while evaluating the Johnson-Cook material constants.

- As the experiments were conducted only at room temperature conditions, temperature variation is zero. So the temperature terms can be ignored. Now the equation narrows down to

$$\sigma = [A + B(\epsilon_P)^n](1 + Cln(\epsilon'^*))$$

- Sample size for every experiment was maintained at a constant. So the strain rate sensitivity term also gets reduced. This narrows down the equation to

$$\sigma = [A + B(\epsilon_P)^n]$$

- The above equation is simple to solve as A parameter being the yield strength which can be interpreted from the stress-strain curve
- Plot the true stress-true strain curve after converting them from engineering stress-engineering strain data.
- Determine the yield strength by 0.2% offset method. This gives us the parameter A required for the equation.
- Extract the plastic part of the stress-strain curve.
- Now the equation can be reduced to

$$\sigma - A = B(\epsilon_P)^n$$

$$ln(\sigma - A) = ln(B(\epsilon_P)^n)$$

- Here $ln(\epsilon_p)$ is plotted along x-axis and $ln(\sigma - A)$ along the y-axis. The slope of the curve gives us parameter n and the intercept gives us $\ln B$. By taking the exponential of the term, B can be extracted.

Table 6.1: Variation in Johnson-Cook parameters with change in strain rate

Strain rate(s^{-1})	A(MPa)	B(MPa)	n
625	1058.6 ±58.6	1591.8 ± 346.8	0.7 ± 0.023
1250	1157.4 ±78.82	2615.7 ± 454.47	0.97 ± 0.115

Table 6.1 tabulates the the constants for simplified Johnson-Cook model extracted from above mentioned steps. Usually, researchers use the linear least square fit method to extract the parameters which can cause inaccuracy with the obtained values as the constants are based on initial guesses which can give rise to human error. By this approach, all constants obtained are almost exact. The reported value of yield strength, strain hardening modulus, and the strain hardening exponent for both strain rates of $625s^{-1}$ and $1250s^{-1}$ are obtained by an average of five experiments conducted at the same strain rate. With the increase in strain rate, there is an increase in yield strength which can be because of increase in strain rate impedes the movement of dislocations which in turn results in an increase in the yield strength. A similar phenomenon is observed also concerning strain hardening modulus and strain hardening exponent. This can be because of the strain rate sensitivity of the material. This phenomenon can be understood better by studying the work hardening rate and strain rate sensitivity plots which will be presented in the manuscript.

Figure 6.7- Figure 6.9 depicts the variation of yield strength, strain hardening modulus, and strain hardening exponent with variation in strain rate from $625s^{-1}$ to 1250 s^{-1} with its error values. Figure 6.10 shows the experimental curve covering only the region after the yield point (i.e.) the plastic part of the stress-strain curve vs the upper and lower bound of obtained material constants from the simplified version of Johnson-Cook model. With this method of extraction, it is proven that both upper and lower bound values agree with the experimental flow stress curve proving the values to be accurately predicted. Strain rate sensitivity and work hardening

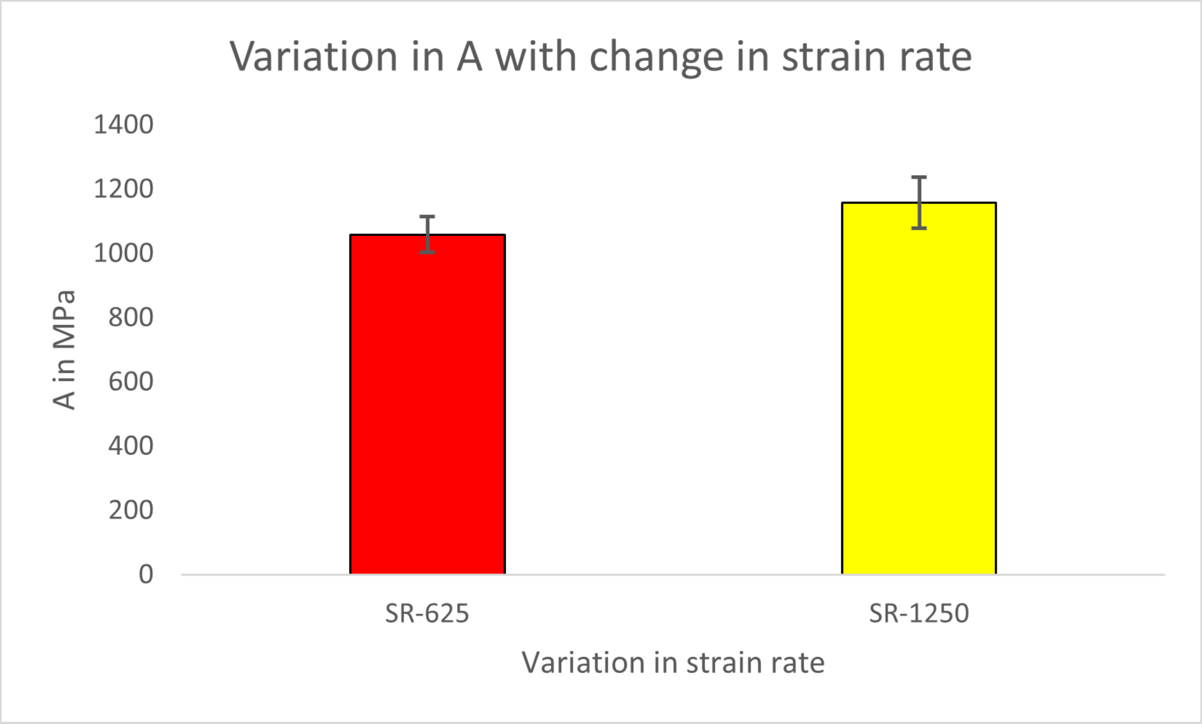

Figure 6.7: Variation of Yield strength with variation in strain rate

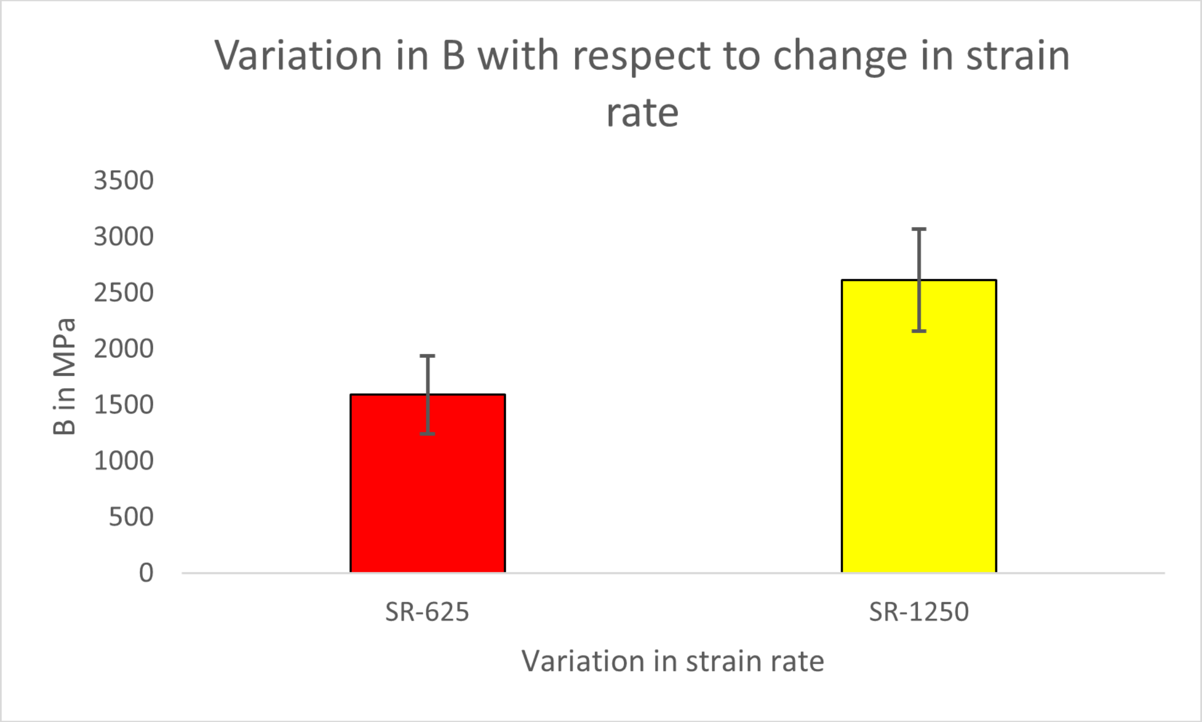

Figure 6.8: Variation of Strain hardening modulus with variation in strain rate

rate will be separately studied to confirm the behavior of Johnson-Cook model parameters in

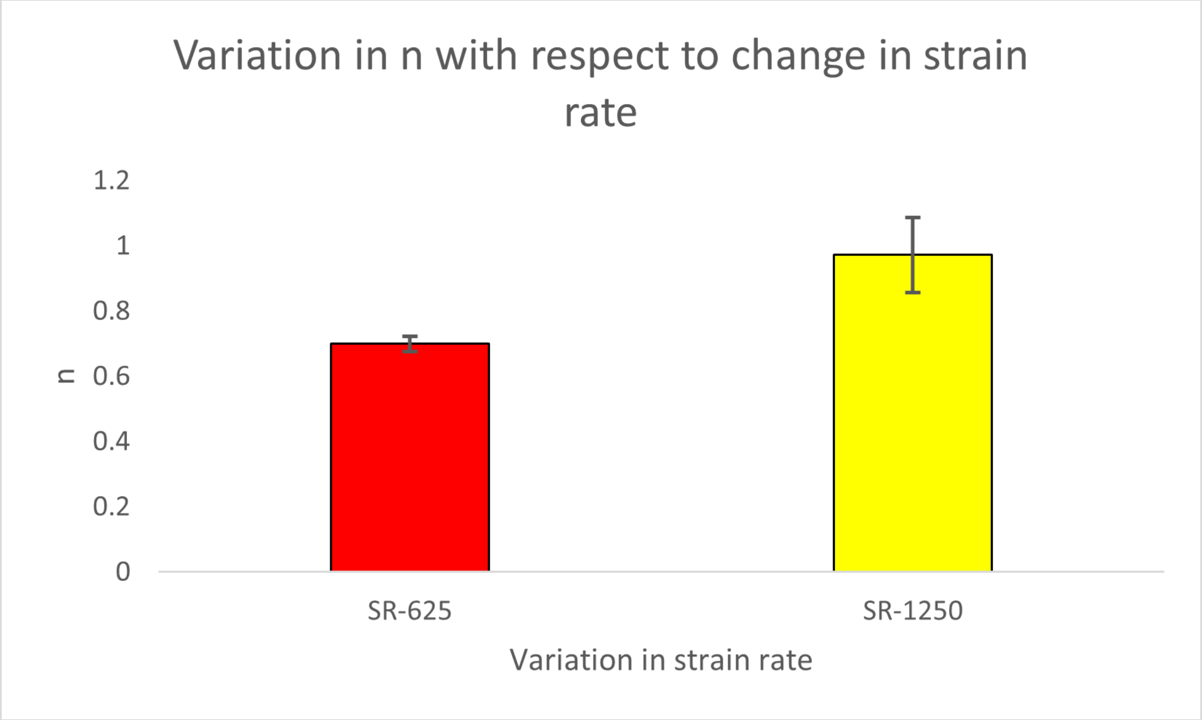

Figure 6.9: Variation of Strain hardening exponent with variation in strain rate

future work. Efforts to study the microstructure have been taken and will be presented in future manuscript works.

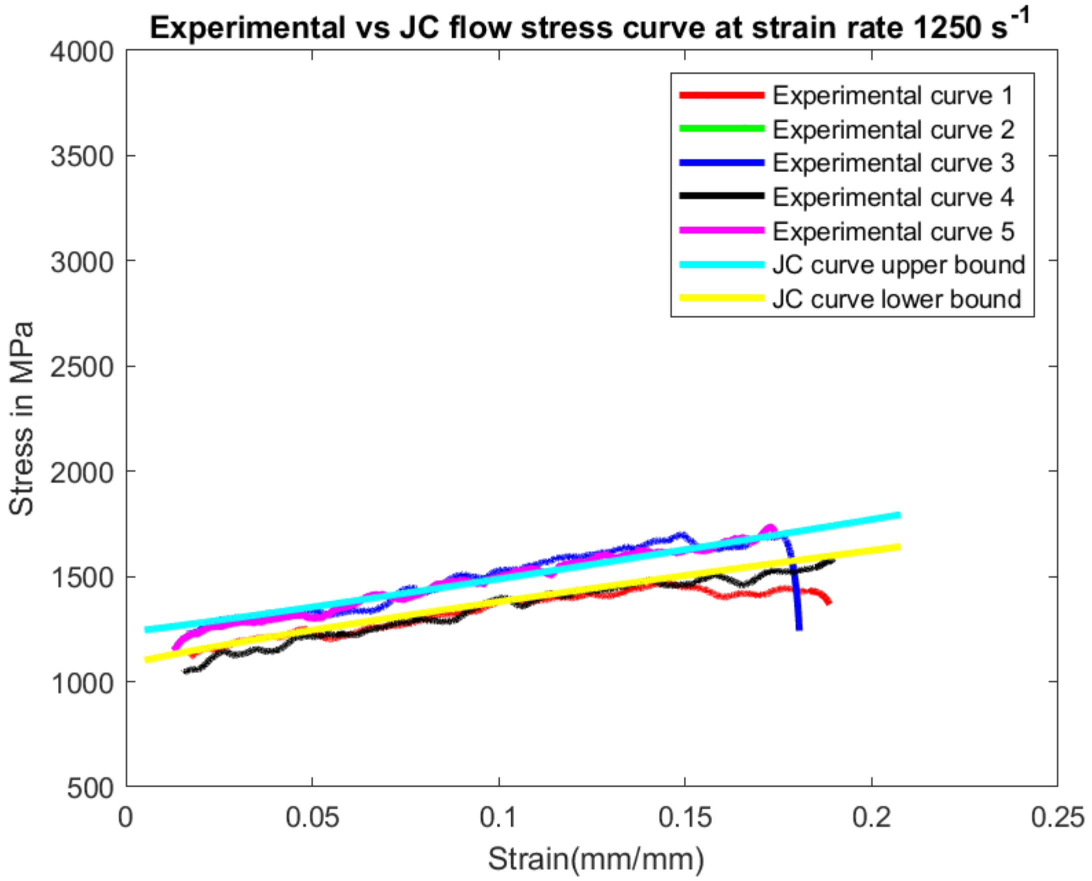

Figure 6.10: JC curve upper and lower bound vs Plastic region of experimental true stress-true strain curve

Chapter 7

Conclusion

7.1 Laser Powder Bed Fusion

17-4 PH stainless steel was fabricated using a laser powder bed fusion process and evaluated under dynamic compression conditions using a split hopkinson pressure bar setup(SHPB). The fabricated specimens are subjected to heat treatment with five variations with one set being as printed condition. The dynamic compression test is conducted under room temperature conditions and at a constant strain rate with the dimensions of the material tested being constant throughout the experiments. Engineering stress-engineering strain data are obtained from the oscilloscope which is in turn connected to the strain gauges bonded on the incident and transmission bar. The obtained engineering stress-engineering strain curve is converted to true stress-true strain data. From the experiment following conclusions were arrived

- At no heat-treated condition, the yield strength of the material is lower due to the presence of defects like porosity and voids which act as a failure point for degradation of yield strength

- With the heat treatment process, the microstructure transitions from a defected structure to semi-recrystallized and finally attains recrystallized microstructures which are responsible for the enhancement of yield strength. During the heat recrystallization process, precipitates are formed on the grain boundaries which contribute to the enhancement of yield strength.

- The original Johnson-Cook(JC) equation is reduced since strain rates and temperature were maintained a constant during experiments.

- The constants were extracted and compared with the experimental stress-strain data.
- It was seen that the obtained constants coincide with the experimental curve with minimal deviation.
- From the obtained JC constants, it was evident that heat treatment does influence the yield strength and the hardening behavior of additively manufactured material.

7.2 Fused Filament Fabrication

17-4 PH stainless steel was fabricated using a fused filament fabrication process and evaluated under quasi-static and dynamic compression conditions using a universal testing machine for quasi-static compression and a Kolsky compression bar for dynamic compression test. The fabricated specimens are subjected to compression tests under varying strain rates The dynamic compression test is conducted under room temperature conditions and varying strain rates with changes in the length of the specimen. Engineering stress-engineering strain data are obtained from the oscilloscope which is in turn connected to the strain gauges bonded on the incident and transmission bar. The obtained engineering stress-engineering strain curve is converted to true stress-true strain data. From the experiment following conclusions were arrived

- Examining the green samples using XCT for porosity distribution, the components are fragile and not rigid enough. The porosity observed in the green sample is higher.
- With the sintering process, the polymer in the hybrid filament evaporates shrinking the metal alone forming the final part which has reduced porosity compared to the green part.
- Quasi-static and dynamic compression tests are conducted on the samples with varying strain rates.
- The original Johnson-Cook(JC) equation is reduced because strain rates and temperature were maintained a constant during experiments.
- The constants were extracted and compared with the experimental stress-strain data.

- It was seen that the obtained constants coincide with the experimental curve with minimal deviation.
- From the obtained JC constants, it was evident that strain rate does influence the yield strength and the hardening behavior of additively manufactured material.

Bibliography

[1] Olaf Andersen et al. "Manufacturing and properties of metal parts made by fused filament fabrication". In: *Euro PM2018 Proceedings. EPMA, Bilbao, Spain* (2018), pp. 14–18.

[2] Mohsen Attaran. "The rise of 3-D printing: The advantages of additive manufacturing over traditional manufacturing". In: *Business horizons* 60.5 (2017), pp. 677–688.

[3] Priyanshu Bajaj et al. "Steels in additive manufacturing: A review of their microstructure and properties". In: *Materials Science and Engineering: A* 772 (2020), p. 138633.

[4] Pere Barriobero-Vila et al. "Peritectic titanium alloys for 3D printing". In: *Nature communications* 9.1 (2018), p. 3426.

[5] Carter Baxter et al. "Constitutive models for the dynamic behaviour of direct metal laser sintered AlSi10Mg_200C under high strain rate shock loading". In: *Materials Science and Engineering: A* 731 (2018), pp. 296–308.

[6] Miguel Ángel Caminero et al. "Effects of fused filament fabrication parameters on the manufacturing of 316L stainless-steel components: geometric and mechanical properties". In: *Rapid Prototyping Journal* 28.10 (2022), pp. 2004–2026.

[7] JA Cherry et al. "Investigation into the effect of process parameters on microstructural and physical properties of 316L stainless steel parts by selective laser melting". In: *The International Journal of Advanced Manufacturing Technology* 76 (2015), pp. 869–879.

[8] Sasan Dadbakhsh et al. "Texture and anisotropy in selective laser melting of NiTi alloy". In: *Materials Science and Engineering: A* 650 (2016), pp. 225–232.

[9] Tarasankar DebRoy et al. “Additive manufacturing of metallic components–process, structure and properties”. In: *Progress in Materials Science* 92 (2018), pp. 112–224.

[10] C Fox et al. “Dynamic Constitutive Behavior of Additively Manufactured 17-4PH Stainless Steel”. In: *Journal of Dynamic Behavior of Materials* 8.2 (2022), pp. 242–254.

[11] JA Gonzalez et al. “Characterization of Inconel 625 fabricated using powder-bed-based additive manufacturing technologies”. In: *Journal of Materials Processing Technology* 264 (2019), pp. 200–210.

[12] Dongdong Gu and Yifu Shen. “Balling phenomena in direct laser sintering of stainless steel powder: Metallurgical mechanisms and control methods”. In: *Materials & Design* 30.8 (2009), pp. 2903–2910.

[13] Murali Mohan Gurusamy and Balkrishna C Rao. “On the performance of modified Zerilli-Armstrong constitutive model in simulating the metal-cutting process”. In: *Journal of Manufacturing Processes* 28 (2017), pp. 253–265.

[14] N Jeyaprakash, Che-Hua Yang, and KR Ramkumar. “Microstructural, mechanical and wear behaviour of Inconel-718 produced through laser-powder bed-fused additive manufacturing”. In: *Materials Science and Technology* 37.3 (2021), pp. 326–337.

[15] Qing Ji et al. “Mechanical properties and a constitutive model of 3D-printed copper powder-filled PLA material”. In: *Polymers* 13.20 (2021), p. 3605.

[16] Gordon R Johnson. “A Constitutive Model and Date for Metals Subject to Large Strains, High Strain Rate and High Temperatures”. In: *Proc. of 7th Int. Symp. on Ballistics, The Hague*. 1983.

[17] GM Karthik et al. “Role of cellular structure on deformation twinning and hetero-deformation induced strengthening of laser powder-bed fusion processed CuSn alloy”. In: *Additive Manufacturing* 54 (2022), p. 102744.

[18] Herbert Kolsky. “An investigation of the mechanical properties of materials at very high rates of loading”. In: *Proceedings of the physical society. Section B* 62.11 (1949), p. 676.

[19] Jean-Pierre Kruth et al. “Lasers and materials in selective laser sintering”. In: *Assembly Automation* 23.4 (2003), pp. 357–371.

[20] Fulvio Lavecchia, Alessandro Pellegrini, and Luigi Maria Galantucci. “Comparative study on the properties of 17-4 PH stainless steel parts made by metal fused filament fabrication process and atomic diffusion additive manufacturing”. In: *Rapid Prototyping Journal* 29.2 (2023), pp. 393–407.

[21] Hong–Ying Li et al. “A modified Johnson Cook model for elevated temperature flow behavior of T24 steel”. In: *Materials Science and Engineering: A* 577 (2013), pp. 138–146.

[22] Xihe Liu et al. “CNT-reinforced AlSi10Mg composite by selective laser melting: microstructural and mechanical properties”. In: *Materials Science and Technology* 35.9 (2019), pp. 1038–1045.

[23] John H Martin et al. “3D printing of high-strength aluminium alloys”. In: *Nature* 549.7672 (2017), pp. 365–369.

[24] Lawrence E Murr et al. “Microstructures and properties of 17-4 PH stainless steel fabricated by selective laser melting”. In: *Journal of Materials Research and Technology* 1.3 (2012), pp. 167–177.

[25] Mahmoud Naim et al. “Effect of post-treatments on the tribological and corrosion behavior of 17-4PH stainless steel processed via fused filament fabrication”. In: *Additive Manufacturing Letters* (2023), p. 100158.

[26] PD Nezhadfar et al. “Fatigue crack growth behavior of additively manufactured 17-4 PH stainless steel: Effects of build orientation and microstructure”. In: *International Journal of Fatigue* 123 (2019), pp. 168–179.

[27] Aghnia Ilmiah Nurhudan et al. “Additive manufacturing of metallic based on extrusion process: A review”. In: *Journal of Manufacturing Processes* 66 (2021), pp. 228–237.

[28] Richard Piola et al. “Antifouling performance of copper-containing fused filament fabrication (FFF) 3-D printing polymer filaments for marine applications”. In: *Biofouling* 37.2 (2021), pp. 206–221.

[29] S Riecker et al. “3D printing of metal parts by means of fused filament fabrication-a non beam-based approach”. In: (2017).

[30] Simone Romano et al. “High cycle fatigue behavior and life prediction for additively manufactured 17-4 PH stainless steel: Effect of sub-surface porosity and surface roughness”. In: *Theoretical and Applied Fracture Mechanics* 106 (2020), p. 102477.

[31] S Sabooni et al. “Laser powder bed fusion of 17–4 PH stainless steel: A comparative study on the effect of heat treatment on the microstructure evolution and mechanical properties”. In: *Additive Manufacturing* 46 (2021), p. 102176.

[32] M Sadaf, M Bragaglia, and F Nanni. *A simple route for additive manufacturing of 316L stainless steel via Fused Filament Fabrication. J Manuf Process 67: 141–150.* 2021.

[33] MK Samal and S Sharma. “A new procedure to evaluate parameters of Johnson–Cook elastic–plastic material model from varying strain rate split Hopkinson pressure bar tests”. In: *Journal of Materials Engineering and Performance* 30 (2021), pp. 8500–8514.

[34] F Sausto et al. “Fatigue failure mechanisms for AlSi10Mg manufactured by L-PBF under axial and torsional loads: The role of defects and residual stresses”. In: *International Journal of Fatigue* 162 (2022), p. 106903.

[35] Paramjot Singh et al. “Printability studies of Ti-6Al-4V by metal fused filament fabrication (MF3)”. In: *International Journal of Refractory Metals and Hard Materials* 91 (2020), p. 105249.

[36] Arash Soltani-Tehrani, Jonathan Pegues, and Nima Shamsaei. “Fatigue behavior of additively manufactured 17-4 PH stainless steel: The effects of part location and powder re-use”. In: *Additive Manufacturing* 36 (2020), p. 101398.

[37] Xu Song et al. “Metal-based 3D-printed micro parts & structures”. In: (2022).

[38] Yu Sun, Rainer J Hebert, and Mark Aindow. “Effect of heat treatments on microstructural evolution of additively manufactured and wrought 17-4PH stainless steel”. In: *Materials & Design* 156 (2018), pp. 429–440.

[39] Lore Thijs et al. “Strong morphological and crystallographic texture and resulting yield strength anisotropy in selective laser melted tantalum”. In: *Acta Materialia* 61.12 (2013), pp. 4657–4668.

[40] Yvonne Thompson et al. “Fused filament fabrication, debinding and sintering as a low cost additive manufacturing method of 316L stainless steel”. In: *Additive Manufacturing* 30 (2019), p. 100861.

[41] CJ Todaro et al. “Grain structure control during metal 3D printing by high-intensity ultrasound”. In: *Nature communications* 11.1 (2020), p. 142.

[42] Claudio Tosto et al. “Fused deposition modeling parameter optimization for cost-effective metal Part Printing”. In: *Polymers* 14.16 (2022), p. 3264.

[43] S Uffelmann and S Pestotnik. “Investigation of the manufacturability of a copper coil for use in space components by means of the fused filament fabrication process”. In: *CEAS Space Journal* 15.5 (2023), pp. 701–713.

[44] Thomas Vilaro, Christophe Colin, and Jean-Dominique Bartout. “As-fabricated and heat-treated microstructures of the Ti-6Al-4V alloy processed by selective laser melting”. In: *Metallurgical and materials transactions A* 42.10 (2011), pp. 3190–3199.

[45] George Z Voyiadjis and Farid H Abed. “Microstructural based models for bcc and fcc metals with temperature and strain rate dependency”. In: *Mechanics of Materials* 37.2-3 (2005), pp. 355–378.

[46] Bey Vrancken et al. “Heat treatment of Ti6Al4V produced by Selective Laser Melting: Microstructure and mechanical properties”. In: *Journal of Alloys and Compounds* 541 (2012), pp. 177–185.